Computational Design and Evaluation of a Smart Material Morphing Building Surface Tile

by

Robert Joseph Zupan Jr.

Bachelor's in Civil Engineering, University of Pittsburgh, 2014

Submitted to the Graduate Faculty of

the Swanson School of Engineering in partial fulfillment

of the requirements for the degree of

Doctor of Philosophy

University of Pittsburgh

2019

UNIVERSITY OF PITTSBURGH

SWANSON SCHOOL OF ENGINEERING

This dissertation was presented

by

Robert Joseph Zupan Jr.

It was defended on

March 27, 2019

and approved by

John C. Brigham, Ph.D., Associate Professor Department of Engineering, Durham University

Julie Vandenbossche, Ph.D., Associate Professor Department of Civil and Environmental Engineering

Lev Khazanovich, Ph.D., Professor Department of Civil and Environmental Engineering

Richard V. Beblo, Ph.D., Research Engineer Air Force Research Laboratory Dayton, OH

Dale Clifford, Ph.D., Associate Professor California Polytechnic State University

Dissertation Director: John C. Brigham, Ph.D., Associate Professor Department of Engineering, Durham University

Computational Design and Evaluation of a Smart Material Morphing Building Surface Tile

Robert Joseph Zupan Jr., PhD

University of Pittsburgh, 2019

The objective of the present work is to develop and numerically evaluate a novel concept for a shape-changing smart material building surface tile. This concept is based on a unique objective to reduce the area of the façade exposed to solar irradiance, thereby reducing thermal gains during high-temperature periods, by intelligently changing the shape of the facade surface depending upon the surface location, time of year, and other environmental factors. Moreover, a particularly high level of control, and therefore functionality is achieved for this tile concept by using a combination of localized smart material activation and mechanical actuation.

First, an evaluation of the self-shading capabilities of the tile concept is presented. Of particular importance is that a morphing tile leads to an increase in shaded area on a building façade in comparison to a static tile. Next, a computational strategy for the design of the morphing tile concept that includes a numerical representation of the tile concept combined with a non-linear optimization process is presented. The computational design approach is shown to be capable of accurately determining design solutions for various target shapes while also minimizing energy usage. Furthermore, it is shown that utilization of a localized material activation (as opposed to global material activation) parameterization leads to more accurate and energy efficient solutions. Finally, the development and quantification of the capabilities of a benchtop prototype of the tile concept is presented. The results indicate that if provided the proper material activation parameters the shape-changing smart material tile can provide a significant decrease in tile area exposed to solar irradiance for various times of day. Furthermore, results indicate that the morphing frequency (i.e., monthly, daily, hourly, etc.) and the control method of an array of tiles (independent vs dependent) have a significant effect on the area of the tile exposed to solar irradiance.

Keywords: Smart Material, Optimization, Self-Shading, Computational Mechanics.

Table of Contents

List of Tables

List of Figures

Preface

First and foremost I would like to express my deepest thanks to my advisor and chair of my graduate committee Dr. John C. Brigham. My success within my work would not have been possible without his guidance and infinite patience.

My thanks to Dr. Rich Beblo and Dr. Dale Clifford as well for their unending help, support, and effort as well as serving on my graduate committee.

I would also like to thank Professors Julie Vandenbossche and Lev Khazanovich for serving on my graduate committee and their support through my studies.

I also give thanks to the professors and administrators of the department of civil engineering at the University of Pittsburgh for supporting, teaching, and helping me for the last eight and a half years.

Finally, I want to thank my family and friends for their unending love and support. In particular, I am grateful for my mother and father's strength, support, and love, my siblings' faith and support, and all my friends' humor, companionship, and unending good times.

1.0 Introduction

There is a significant amount of work to develop responsive building technologies, specifically those that interact with and respond to the environment to increase the energy efficiency of the building. A portion of these responsive building technologies have investigated the use of smart materials due to their capabilities to alter material properties based on external stimuli. However, thus far only a small number of responsive building technologies have utilized smart materials, and there are many potential capabilities of smart materials and uses for responsive building technologies that have not yet been considered. The objective of the present work is to develop and numerically evaluate a novel concept for a shape-changing smart material building surface tile. This concept is based on a unique objective to reduce the area of the façade exposed to solar irradiance, thereby reducing thermal gains during high-temperature periods, by intelligently changing the shape of the facade surface depending upon the surface location, time of year, and other environmental factors. Moreover, a particularly high level of control, and therefore functionality is achieved for this tile concept by using a combination of localized smart material activation and mechanical actuation.

The development of the smart material building surface tile design concept can be divided into three key focuses: (1) the evaluation of the self-shading capabilities of a dynamically shape-changing tile as a building surface component, (2) the development of a computational strategy for design and control of a shape-changing smart material tile, and (3) the development and quantification of the capabilities of a benchtop prototype of the tile concept. For the first focus, numerical case studies are shown that quantify the shading capabilities of various static and dynamic tile shapes at different locations on a building to identify features of "wrinkle" patterns that positively affect self-shading. Additionally, numerical case studies are shown that quantify the trade-off between self-shaded area and a morphing cost metric. Of particular importance is that a dynamically changing tile leads to an increase in shaded area on a building façade in comparison to a static tile. Additionally, the amount of shading decreases significantly after a certain number of morphs (three morphs for the cases considered). For the second focus, a computational approach is developed that utilizes

a shape-based optimization procedure to determine the optimal morphing mechanisms to minimize the shape difference between a target surface and a numerically estimated surface. Within the computational design approach several shape-based objective functions and multiple morphing mechanism parameterizations are considered in numerical case studies. The computational design approach is shown to be capable of accurately determining design solutions for various target shapes while also minimizing energy usage. Specifically, it is shown that utilization of the Modified Hausdorff distance as an objective (compared to the other objectives considered) more consistently resulted in accurate optimal solutions. Furthermore, it is shown that utilization of a localized material activation (as opposed to global material activation) parameterization leads to more accurate and energy efficient solutions. For the third focus, a benchtop prototype of a three-dimensional (3D) printed smart material (specifically shape memory polymer) tile is developed and an experimental procedure is presented. Physical experiments are shown that evaluate results for both global and localized material activation of the benchtop prototype. A numerical representation of the tile calibrated and validated based on these results is then presented. Numerical tests are shown that investigate the capability of a shape-changing smart material tile to minimize the area of the tile exposed to solar irradiance. The results indicate that if provided the proper material activation parameters the shape-changing smart material tile can provide a significant decrease in tile area exposed to solar irradiance for various times of day. Furthermore, results indicate that the morphing frequency (i.e., monthly, daily, hourly, etc.) and the control method of an array of tiles (independent vs dependent) have a significant effect on the area of the tile exposed to solar irradiance.

2.0 Numerical Investigation of Capabilities for Dynamic Self-Shading through Shape Changing Building Surface Tiles

2.1 Overview

A concept for a smart material morphing building surface tile that would utilize adaptive surface wrinkle patterns to improve solar interaction is explored. The effect of the wrinkle patterns is numerically investigated in the context of an objective to reduce solar irradiance entering buildings by changing the shape of the surface (i.e., surface topography) so that the façade is self-shading, thereby reducing energy costs of the building for temperature control. A generally applicable algorithm was utilized and is presented to quantify the area of an arbitrarily shaped/oriented surface that is in shade for any given date/time and geographic location. Numerical case studies are shown that utilize the self-shading algorithm to evaluate the capabilities of various wrinkle patterns, both static and dynamically changing, to self-shade a building surface throughout a day. The results indicate that a morphing wrinkle pattern can substantially increase the amount and duration of surface area in shade over time in comparison to the static (non-morphing) patterns considered in this study, although it is noted that there is a tradeoff in the energy cost to change the surface pattern. Furthermore, it is shown that as the location of the proposed tile on the building changes, the optimal wrinkle pattern changes as well.

2.2 Introduction

Buildings that can adaptively respond to fluctuating environmental conditions have the proven potential to increase occupant comfort and significantly decrease energy consumption and carbon emissions [1, 2]. Moreover with commercial buildings alone accounting for over 40% of energy consumption in the United States [3], environmentally responsive building technologies for reducing energy consumption are a particularly promising area of collabora-

tive and multidisciplinary research. The main consumers of energy in commercial buildings are lighting, ventilation, and heating and cooling [3]. Therefore, in an effort to increase energy efficiency, many building technologies being developed are focused on optimally regulating these main consumers using a variety of dynamic control systems for lighting [1, 4–6], ventilation [2, 7–9], and cooling [10–12]. These technologies are widely used in commercial buildings, and recently in an effort to further increase energy efficiency researchers have been focusing on utilizing the building envelope[13–15], which includes the façade, roof, and windows.

Technologies utilizing the building envelope, such as the façade, have been shown to affect the energy demand of commercial buildings [16–19]. These technologies have the ability to affect ventilation, interior lighting, and wind drag by utilizing varying porosity [20, 21], light filtering [12], and varying surface texture[22]. The present work focuses on environmentally responsive exterior shading. Controlling how the building interacts with sunlight has the potential to reduce both lighting and heating and cooling costs. Examples of exterior building components that focus specifically on interaction with light that have been proposed include external louvers and awnings/overhangs [23–27], photovoltaic panels [28–31], and building surface skins [32–38].

Of the adaptive building envelope technologies in existence and under development, many utilize smart materials to facilitate the adaptive behavior. A recent example is the proposed use of hygromorphic materials to create an adaptive structure concept that is inspired by the opening and closing of the surface elements of conifer cones [39]. Alternatively, Barrett and coworkers [35–37] have been developing a device that is likely most similar to the concept proposed herein, in terms of both objective and mechanism. Barrett et al. have proposed a smart material building covering, called "Thermadapt", that would change shape based on thermal loading throughout the day. To achieve the surface morphing the building coverings take advantage of coefficient of thermal expansion (CTE) mismatch. The building covering has an outer layer with a lower CTE than the inner layer, therefore when the temperature rises the inner layer expands first, causing the building covering to curve outwards, altering the shape of the exterior into a self-shading configuration. The inner layer would also be the first to contract in cold weather, causing the building coverings to curve inwards, providing

insulation by trapping air pockets under the coverings. This building covering technology has been shown to lead to peak temperatures $10-14^\circ$ F lower than ambient peak temperatures. It also performs well in cold temperatures, showing similar temperatures as standard insulation while using much less material. On a larger scale, Capeluto investigated the effects of utilizing a larger portion of the building envelope for self-shading purposes and showed similar positive results [40].

The present work proposes a building surface tile that (similarly to Barrett's work) self-shades the surface to affect the solar irradiance entering the building. In contrast, the approach for self-shading is based upon a technology previously explored by Clifford referred to as "cactus tiles" [41]. The cactus tile is a bio-inspired form for a building surface, that is based on the skin of a cactus, which has extensive wrinkling that functions to self-shade the cactus and prevent it from overheating in the sun, this effect was explored previously by Ehleringer [42]. Preliminary tests showed that on a 100° F day on a South facing façade, a wrinkled building surface was 30° F cooler than a surrounding unshaded brick surface, substantially lowering thermal transfer to the building interior. However, this concept was initially envisioned to be static (i.e., the wrinkle pattern of the building surface would be the same year-round), and would not account for changes in the angle/direction of sunlight or changes in the self-shading (i.e., cooling) demand throughout a day and year. As such, the present study intends to explore the potential of a morphing cactus tile that has a dynamically changing wrinkle pattern, which could control the level of self-shading provided by the façade based upon the time of day and/or season. The key difference between the proposed technology and the technologies developed by Barrett [35–37], Nagy [38], and others is that the proposed technology has a continuous deformable surface while the others simply have discrete elements with limited range of motion. Therefore, it is expected that the proposed technology will have a design space with a higher number of solutions, potentially leading to greater efficiency or functionality.

To evaluate the potential of this morphing cactus tile concept and to motivate future efforts to develop the technology, a set of numerical case studies were investigated regarding the self-shading capability of various static and dynamic cactus tiles surface topographies. First, it was necessary to identify and utilize an algorithm to calculate the portion of a

surface that is self-shaded for any feasible tile (wrinkled) shape, geographic location, and environmental conditions, which is elaborated upon in the following. Then, the case studies are presented, which examine the potential self-shading capabilities of various basic wrinkle pattern possibilities throughout a given day. Lastly, concluding remarks and future directions to further explore the proposed technology are discussed.

An important note is that the potential benefit of having non-flat tile shapes is through the control of how heat is transferred to the building. Specifically, note the fourth-order relationship between thermal radiation and temperature in contrast to the linear relationship of thermal convection and conduction to temperature [43]. For example, if a fixed amount of solar energy is focused on a surface area that is 50% smaller than the original area of the surface, the resulting temperature of the exposed surface area will double. Due to the fourth-order relationship between temperature and thermal radiation this leads to the thermal energy being radiated from the tile to increase by a factor of 16, which in turn reduces the amount of the finite thermal energy being conducted into the building. In this simplified example, radiation and convection are assumed wholly exterior phenomena.

2.3 Algorithm for Quantification of Self-Shading of an Arbitrary Surface

Most applications requiring quantification of shaded area of a surface have largely focused on structured shapes, such as overhangs, awnings, and louvers [23–27, 44, 45]. As such, the algorithms utilized therein are not applicable to arbitrarily shaped surfaces as are considered here for the morphing building surface tile concept, and a more generalized algorithm is needed. Rendering technology, such as Radiosity [46, 47], use algorithms capable of calculating the area of shaded area of arbitrarily shaped surfaces. Therefore an algorithm, similar to those used in such technologies, was modified to be applicable to a shape defined by a finite element mesh.

The shading quantification algorithm utilized assumes that the surface to be evaluated be defined by a standard finite element-type mesh, based upon a set of nodes and their connectivity as elements. Then, all that is necessary is to determine the state of shading

of each element, using a form of backwards ray tracing, and numerically integrate over the mesh to determine the total area that is self-shaded for the given arbitrarily shaped surface. As such, the algorithm utilized to quantify the self-shading of an arbitrary surface can be described as follows:

INPUT: nodal coordinates and element connectivity of mesh description of surface, latitude, longitude, and elevation of the surface location, date, and time.

1. Calculate Azimuth and Zenith angles of the sun's position relative to the surface (as detailed in the following).

2. Loop over each element in the mesh, and for each element:

    a. Determine the centroid of the element

    b. Determine the direction (vector) of a solar ray that passes through the centroid.

    c. Determine if any other element in the mesh intersects the solar ray vector (i.e., shading the current element).

    d. If the solar ray vector intersects any other element (between current element and sun), then add the current element area to the total shaded area sum.

A critical element of any approach to shading quantification (including the algorithm utilized herein) is calculation of the solar position at the point in space and time on the surface of interest. There are numerous methods to determine solar position, characterized by the zenith (or elevation) and azimuth angles [48–50]. The algorithm used in the present effort is the Solar Position Algorithm (SPA) developed in [48]. SPA was chosen because of the relatively high accuracy compared to other options, with maximum uncertainties in the calculated angles of $\pm 0.0003\,^{\circ}$. As detailed in [48], SPA requires the location (latitude and longitude), date, time, and spatial and temporal properties of the location (elevation, average annual temp/pressure, etc.), and outputs several solar position measures, including those required for the self-shading quantification algorithm herein of the zenith and azimuth angles. The unit vector of the solar ray can then be characterized using the zenith and

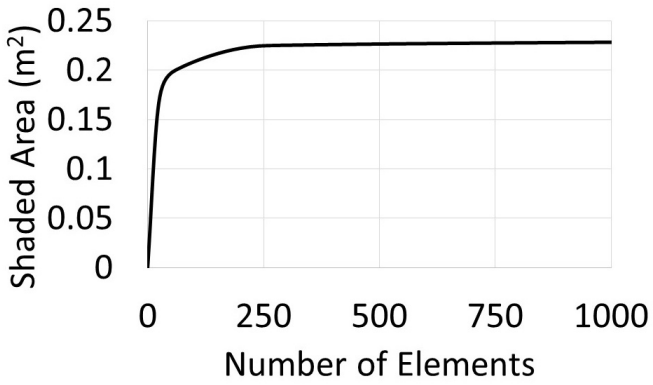

Figure 2.1: Number of elements (mesh size) with respect to shaded area of a vertical wall shaded by an overhang.

azimuth angles as:

$$v_s = \begin{bmatrix} \cos(\gamma_s) * \cos(\alpha_s) \\ -\cos(\gamma_s) * \sin(\alpha_s) \\ \sin(\gamma_s) \end{bmatrix}, \tag{2.1}$$

where γ_s is the elevation angle (degrees), α_s is the azimuth angle relative to South (degrees), North is positive x, West is positive y, and height is positive z.

A final component to an algorithm such as this is to perform a mesh convergence analysis to ensure that the mesh utilized to produce the final result is sufficiently small for the result to be accurate. A basic overhang shape, with a 1 m by 1 m wall and a 1 m by 0.25 m overhang, was considered for a convergence study. Figure 2.1 shows the number of elements with respect to shaded area for the overhang shape. Figure 2.2 Shows a visual representation of the convergence process. As shown in Figure 2.2, for an example self-shading calculation the algorithm would be repeated with sequentially more refined meshes until the shading estimate stops significantly changing. As can be seen in the example, the estimates provided by Figure 2.2(c) and Figure 2.2(d) are significantly more similar than either of the prior estimates, and it is likely that the estimate in Figure 2.2(d) is sufficiently converged.

To verify and validate the accuracy of the self-shading algorithm, examples of shading geometries, their locations, and orientations from [45] were evaluated. The first shape considered was the overhang shape shown in Figure 2.3, oriented West at 13:07 on March 10th,

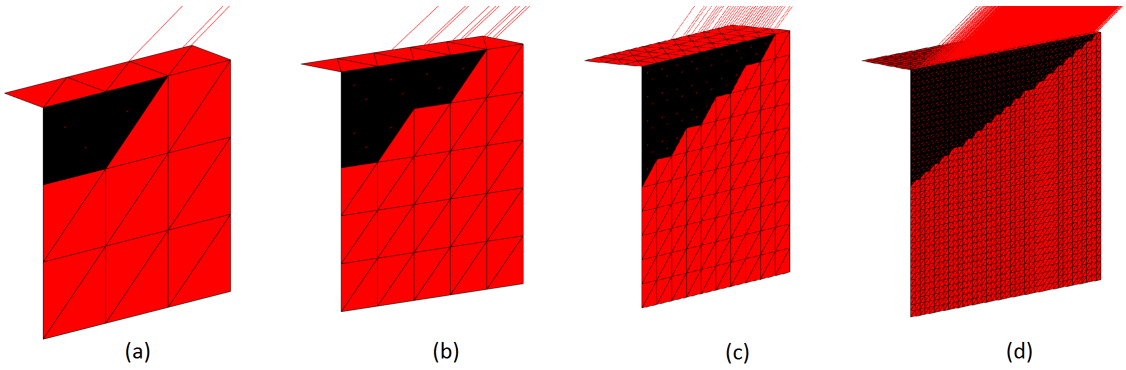

Figure 2.2: Example of the self-shading estimate from the algorithm presented herein for four different levels of mesh refinement (a - d), with shaded elements in black and exposed elements in red.

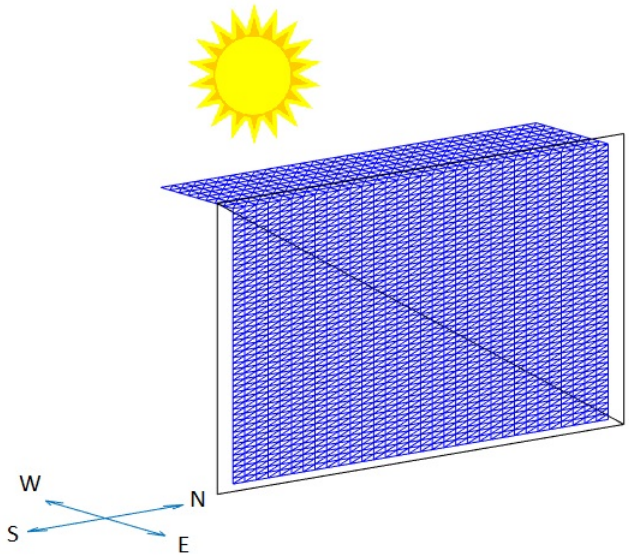

Figure 2.3: Meshed representation of the West facing overhang surface example.

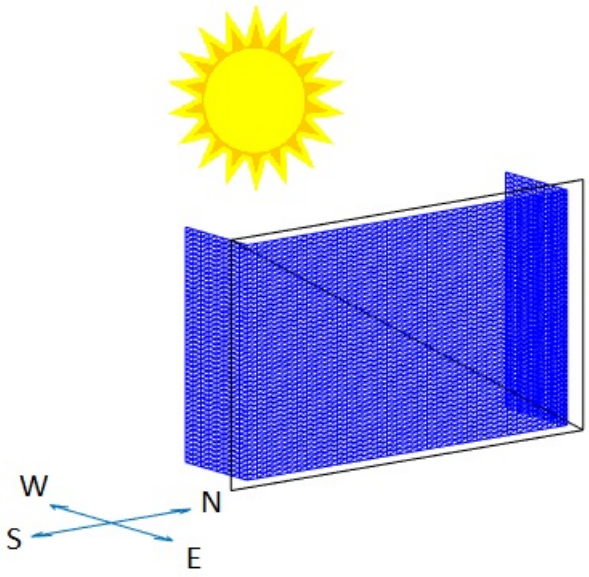

Figure 2.4: Meshed representation of the double vertical fin surface example.

2004. The algorithm was verified by first performing a mesh dependency study, and then comparing to the analytical solution found by projecting the overhang through the solar angle onto the vertical wall and calculating the shaded area using simple geometry. The algorithm converged to a value differing from the analytical solution by 0.1% using 3584 elements, confirming the algorithm converges within acceptable limits.

Finally, to validate the present algorithm, converged estimates of surface shaded area were calculated for two additional test cases from the work in [45] that had corresponding experimental measurements. The two test cases considered were the overhang case with the same location and orientation from the verification test and a double vertical fin device oriented West at 13:36 on March 14th, 2004, as shown in Figure 2.4. The experimental result reported in [45] for the overhang case was 75% shaded area, in contrast to the 73% predicted by the shading quantification algorithm. Additionally, the shading quantification algorithm estimated a self-shaded area of 17% for the conditions of the double vertical fin case, while the experimental results were 19%. With both example cases resulting in differences between

the experimental and numerical estimates of shading of only 2%, the shading quantification algorithm was considered to have calculated the shaded area of the objects within acceptable limits.

2.4 Self-Shading Numerical Case Studies

Several case studies were numerically investigated with respect to shading potential of the proposed building surface tile concept involving various scenarios for potential tile shapes, orientation, location, and time of day. Overall, these case studies were based upon a single shape-changing tile, covering a 1m by 1m plane area, on a conceptual surface located in Phoenix, Arizona (Lat: 33.45, Long: -112.07) throughout the day of July 4^{th}, 2015, which had an average high of 102°F. It was assumed that the tile would be rigidly held on two of the four edges (e.g., top and bottom or left and right), and with shape changing only occurring through changes in the out-of-plane surface position. It was further assumed that the tile would operate similarly to the previously mentioned technology being developed by Barrett et al. [35–37], with the tile being comprised of a smart material, and the shape change therefore being achieved by deformation of the tile material (rather than mechanical components such as hinges). To address potential material limitations at this stage of the development (i.e., without having selected an optimal smart material for device construction), each shape change considered was normalized for comparability between shapes such that the surface area change with respect to a flat surface was fixed at 150% (i.e., the total surface area of each deformed shape considered was fixed at 1.5 m^2). Although the distribution of this deformation would likely become important in future development, this 150% overall deformation is well within the limits of many smart materials, such as shape memory polymers [51] (commonly shown to exceed 200% recoverable deformation). Furthermore, the normalization allows each shape change to be fairly compared in the sense that the total deformation is equivalent.

For simplicity, three basic wrinkle patterns were considered, which were simplified geometric representations of the previously discussed concept of a "cactus" tile [41]. The three

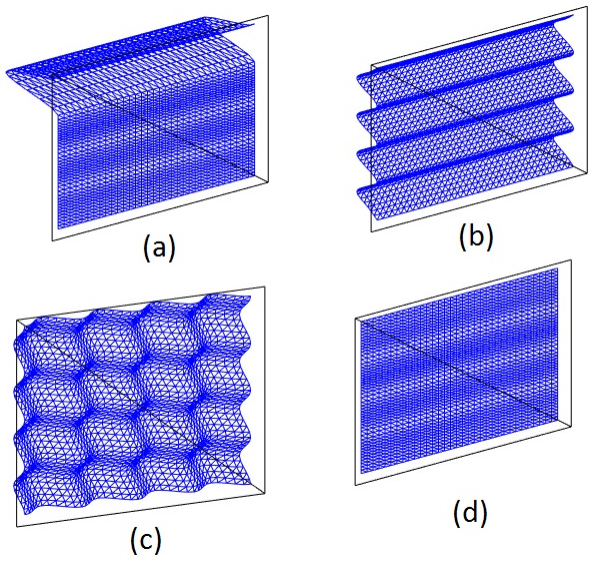

Figure 2.5: Mesh-based surface representation of the (a) single sin-wave overhang, (b) continuous unidirectional sin-wave, (c) continuous bidirectional sin-wave, (d) undeformed tile shapes.

basic wrinkle patterns considered (in addition to the undeformed tile) are shown in Figure 2.5, and are described by the equation for the out-of-plane surface position, z, as
a single sin-wave overhang:

$$z = \begin{cases} A * [\sin(\frac{2*\pi}{P} * (x + \frac{3*P}{4})) + 1] & \text{for } 0 \leq x \leq 4 - P \\ 0 & \text{for } 4 - P < x \leq 4 \end{cases}, \tag{2.2}$$

a continuous unidirectional sin-wave:

$$z = A * \left[\sin\left(\frac{2 * \pi}{P} * \left(x + \frac{3 * P}{4}\right)\right) + 1\right] \quad \text{for } 0 \leq x \leq 4 \tag{2.3}$$

and a continuous bidirectional sin-wave:

$$z = A - \frac{A}{2} * \left[\cos\left(\frac{2 * \pi}{P} * (x - 4)\right) + \cos\left(\frac{2 * \pi}{P} * (y - 4)\right)\right] \quad \text{for } 0 \leq x, y \leq 4 \tag{2.4}$$

where x and y are the in-plane coordinates of the plate, and A and P are the amplitude and period of the sin-wave, respectively.

To quantify the shading potential of each tile scenario over time, the 10-hour period of daylight on the specified date was considered and the surface shading for each tile scenario was calculated each hour on the hour for two conceptual locations on the building, a West facing vertical wall and a South facing roof (45 °). In the following the self-shading potential of these three basic wrinkle patterns is examined individually by evaluating the amount of self-shading for a set of variations (e.g., changes in shape amplitude, etc.) for each basic shape form over the specified 10-hour period. Next, the basic wrinkle patterns are compared to one another in terms of the shading capability. An important note is that this first set of tests considered the tiles to be static (i.e., non-morphing) to evaluate the potential of the shapes. Next, the potential self-shading of a morphing tile is evaluated by considering the capability of the tile to morph between the wrinkle patterns, and considering both shading throughout the day as well as a measure of complexity for the morphing process. Finally, a comparison is made between the results of the two conceptual locations on the building. It should be noted that mesh convergence was confirmed for all shapes.

2.4.1 Shading Potential of the Individual Basic Wrinkle Patterns

The percent of each tile shaded was determined over the specified day for three variations of each shape form for the vertical West wall. The variations in the three basic wrinkle patterns were generated by modifying the values of A and P in (2.2), (2.3), and (2.4). Table 2.1 shows all nine parameter combinations of the basic wrinkle patterns considered. Again, note that the shape variations all maintained the specified total surface area constraint (i.e., increasing the period of the shapes required increasing the amplitude to maintain the 1.5 m^2 surface area).

Figure 2.6 compares the percentage of the tile surface area shaded over time for the variations considered for the overhang basic shape form. The overhang with a period of 0.125 m provides the highest percentage of self-shading until approximately 13:30, then the overhang with a period of 0.250 m temporarily provides the highest shading until approximately 14:30, the overhang with a period of 0.500 m provides the highest percentage from 14:30 to 17:00, at which point the periods of 0.125 m and 0.250 m provide approximately equivalent shading

Table 2.1: The period (P) and amplitude (A) for each of the variations of the wrinkle patterns considered.

Shape:	P (m)	A (m)
Overhang	0.125	0.1550
	0.250	0.1740
	0.500	0.2150
Unidirectional Sin-wave	0.125	0.0342
	0.250	0.0675
	0.500	0.1350
Bidirectional Sin-wave	0.125	0.0975
	0.250	0.1850
	0.500	0.3656

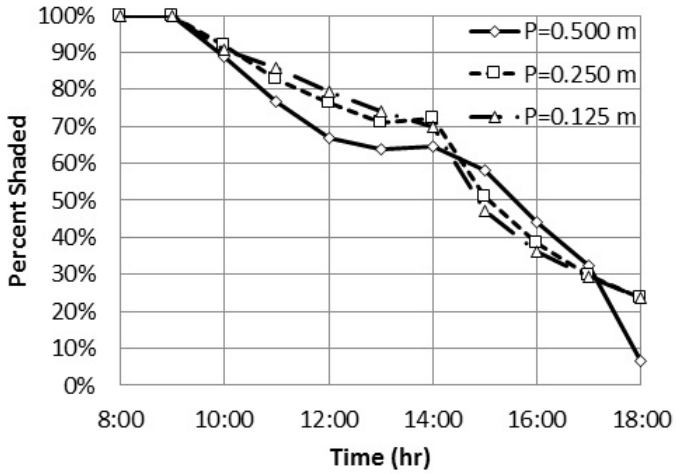

Figure 2.6: Percent of the surface that is self-shaded with respect to the time of day for variations of the period length (P) of the single sin-wave overhang shape.

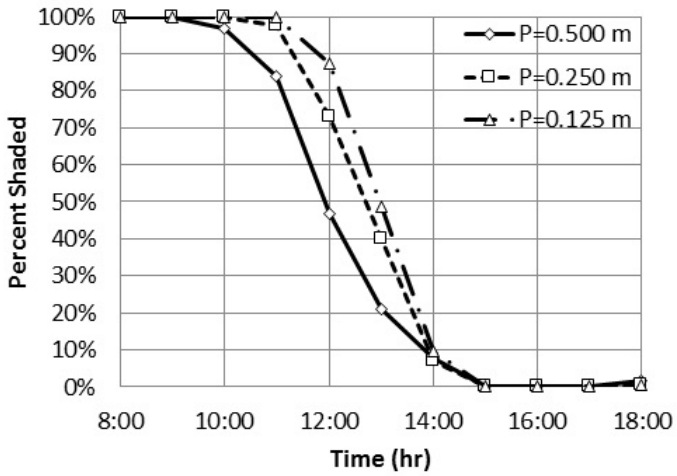

Figure 2.7: Percent of the surface that is self-shaded with respect to the time of day for variations of the period length (P) of the unidirectional sin-wave shape.

for the remainder of the day. Figure 2.7 shows the analogous results for the unidirectional sin-wave. The unidirectional sin-wave with period of 0.125 m provides the highest percentage of self-shading until approximately 14:00, when all three periods considered provide approximately equivalent shading for the remainder of the day. Finally, Figure 2.8 shows percent of the tile shaded over time for the three different parameter combinations of the bidirectional sin-wave shape. Similar to the unidirectional sin-wave, the period of 0.125 m provides the highest self-shading for the first part of the day, until approximately 15:30, and once again the three shape variations remain approximately equivalent for the remainder of the day. Generally, as the period decreased (i.e., the more "wrinkly" the shapes became) the amount of self-shading increased. However, with the limitation on the total surface area, there is a point of diminishing returns when decreasing the period size (which increases the number of shadows), since the amplitude must correspondingly decrease (which decreases each shadow height). Although not shown here for brevity, additional tests indicated that this point of diminishing returns was approximately the amplitude of 0.125 m for the examples herein.

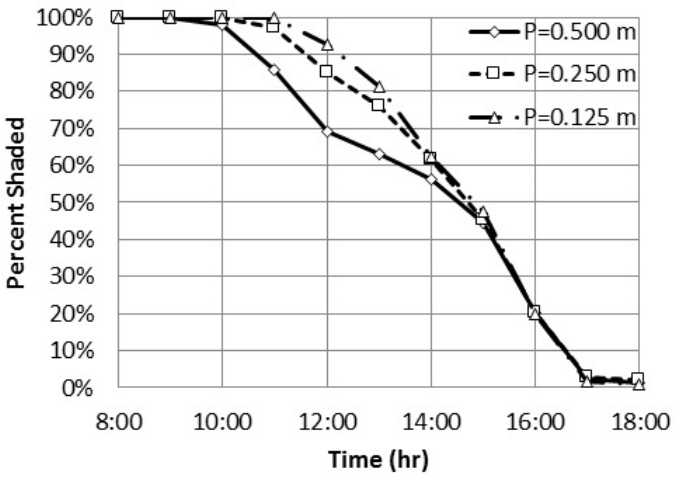

Figure 2.8: Percent of the surface that is self-shaded with respect to the time of day for variations of the period length (P) of the bidirectional sin-wave shape.

Figure 2.9 shows the shading over time for the three basic wrinkle patterns with a period of 0.125 m (i.e., the period with the highest total shading over the day for each). The unidirectional sin-wave had the highest percent shading for a large portion of the day, with the exception of 14:00 and after 16:30 when the overhang shape provided the highest amount of self-shading. More importantly, a general observation from Figures 2.6-2.9 is that none of the basic wrinkle patterns or parameter combinations had a higher amount of self-shading than the others throughout the entirety of the day. In other words, a tile that is able to morph between such shapes and parameter combinations throughout the day would be able to self-shade more of the surface over a longer period of time compared to any static shape considered.

2.4.2 Shading Potential of a Dynamic Tile Shape

To begin evaluation of the potential of a morphing tile, Figure 2.10 shows the optimal combination of the shapes considered in the previous section in terms of maximizing the total shaded area over the day by allowing the tile shape to change every hour compared to the highest total shading static versions (i.e., unchanging) of the basic wrinkle patterns. The morphing tile shades the surface significantly more over the day than any one of the static

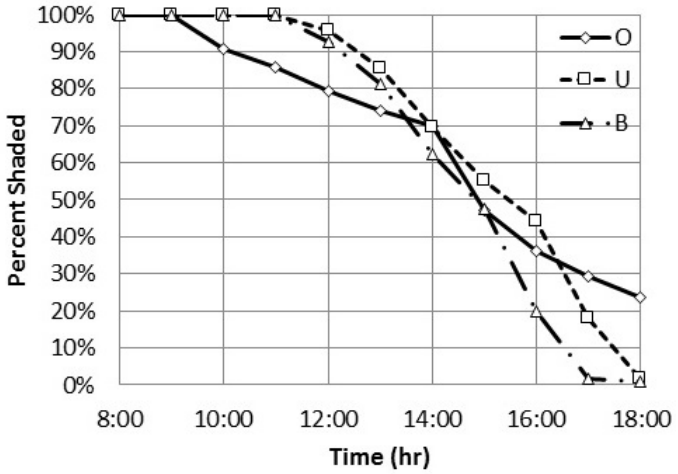

Figure 2.9: Percent of the surface that is self-shaded with respect to time of day for the overhang (O), unidirectional (U), and bidirectional (B) shapes with period length of 0.125 m

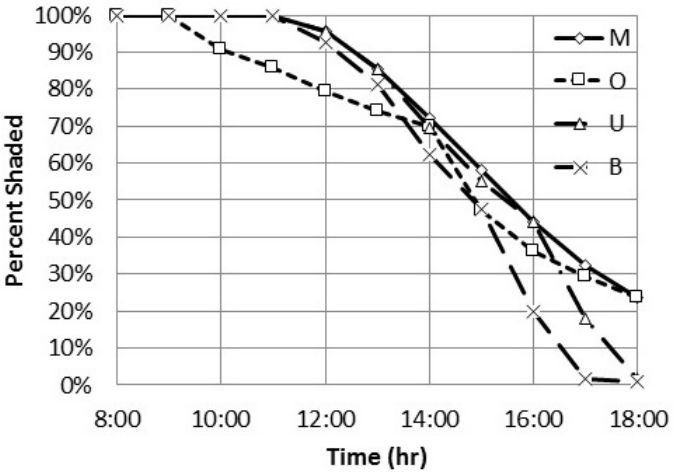

Figure 2.10: Percent of the surface that is self-shaded with respect to time of day for a morphing tile (M) and the overhang (O), unidirectional (U), and bidirectional (B) shapes with period length of 0.125 m.

shapes, with a total percent surface-hours of shade (i.e., area under the percent shaded vs. time curve) of 7.50 compared to the next highest static shape, the unidirectional sin-wave of 7.18. However, an important aspect that has not been discussed to this point is that there is expected to be an energy (or other) cost to morph a surface tile from one shape into another. Therefore, the optimized morphing process shown in Figure 2.10, that requires 5 shape changes, may ultimately have more cost than benefit compared to a tile that changes shape less often in certain circumstances.

It should be again noted that without further developments of the proposed technology the morphing cost cannot be predicted precisely. Depending on the smart material/structure mechanism used, this cost could include energy for activation or actuation of the structure/material or simply the complexity of the build needed to achieve the functionality. To still provide a perspective, it is assumed herein that the cost of performing a shape change is directly proportional to a measure of the difference between the two subsequent tile shapes during the morphing process. Again noting that the hypothetical mechanism for the morphing tiles herein would be deformation (as through the use of a smart material), the amount of deformation (i.e., shape change) is expected to be a reasonable estimate of the relative input energy required to morph. As such, the following metric of the difference between two tile shapes was utilized:

$$D_{i,j} = \left(\int_0^X \int_0^Y (z_i - z_j)^2 dxdy \right)^{\frac{1}{2}} \tag{2.5}$$

where z_i and z_j are the out-of-plane surface positions of the shapes at the i^{th} and j^{th} hour, respectively. The difference metrics for all possible combinations of the shapes considered are displayed in Table 2.2.

Considering both maximization of the percent self-shading and minimization of the cost of morphing over an entire day, selecting the optimal morphing tile can now be thought of as a multiobjective design problem as follows:

$$\text{Minimize: } B^{-1} + \beta * C, \tag{2.6}$$

with

$$B = \int_{8:00}^{18:00} S(t)dt \tag{2.7}$$

Table 2.2: Difference metric, calculated from (2.5), for each combination of shapes considered in the case studies. Note: the matrix presented in this table is symmetric.

		Overhang			Unidirectional Sin-wave			Bidirectional Sin-wave		
	Period (m)	P=0.125	P=0.250	P=0.500	P=0.125	P=0.250	P=0.500	P=0.125	P=0.250	P=0.500
Overhang	P=0.125	0.00	7.01	7.41	4.64	5.40	5.36	5.37	4.93	4.71
	P=0.250		0.00	6.23	5.82	4.50	2.98	4.41	3.18	5.41
	P=0.500			0.00	5.75	1.73	5.71	2.30	5.14	5.53
Unidirectional	P=0.125				0.00	3.07	1.52	3.82	1.78	0.43
	P=0.250					0.00	2.98	1.56	2.61	2.88
	P=0.500						0.00	3.51	0.79	1.32
Bidirectional	P=0.125							0.00	2.99	3.55
	P=0.250								0.00	1.51
	P=0.500									0.00

and

$$C = \sum_{i=1}^{10} D_{i,i+1}, \tag{2.8}$$

where $S(t)$ is the percent shading over time and β is a user-defined parameter to weight the relative importance of the two competing objectives.

To interpret the tradeoff between B^{-1}, units of $(m^2\text{-}h)^{-1}$, and C, units of m, of this morphing tile, the Pareto front was generated for the present example by varying the total number of shape changes over the day (and thus controlling the morphing cost). Figure 2.11(a) shows the value of the two design objectives for each point on the Pareto front and Figure 2.11(b) shows the corresponding sequence of shapes obtained from the shading maximization. The Pareto front shows that there is a substantial tradeoff between the morphing cost (i.e., amount of shape change) and the amount of self-shading provided throughout the day. In particular, there is a nearly linear tradeoff between the cost-benefit of 0 to 3 shape changes over the day (especially 1 to 3 shape changes). Alternatively, the increase in the amount of shading decreases significantly after 3 shape changes, with almost negligible differences in the total shading with 3 shape changes compared to 5 shape changes, but with a substantial increase in the shape change cost. An important reminder, however, is that this design solution set is for one particular tile location/position on a conceptual building, and it is expected that not only different geographic locations, but even different positions

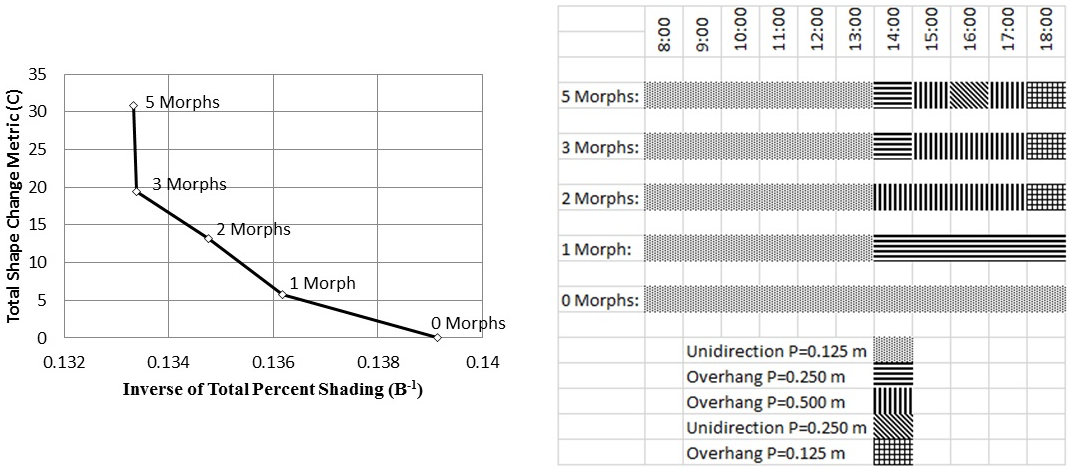

Figure 2.11: (a) The total shape change metric (C) with respect to the inverse of the total percent shading over the day (B^{-1}) and (b) the sequence of shapes for each point on the morphing tile Pareto front.

on the same building would yield different optimal morphing tile systems, as considered in the following. Additionally, this design solution set is for a finite set of shapes and it is expected that allowing the tile to morph to any shape (not just predetermined sets) will allow for even further shading capabilities. Changes in solar irradiation throughout the day are also not included in this analysis, which will have a large impact on the benefit side of the cost-benefit analysis in determining whether or not to morph.

2.4.3 Shading Potential for a Different Morphing Tile Location

To evaluate how a tile's location on the façade might affect the morphing scheme an additional set of numerical tests were carried out. This second set of tests considered a tile at the same geographic location and date as the previous tests, but on a South facing roof façade angled at 45 ° (in contrast to the West facing vertical wall considered previously). For the roof façade, the self-shading throughout the day was calculated for the same basic wrinkle patterns (and variations) that were previously considered. Additionally, for this roof example, each shape form and period variation was considered with the entire surface rotated in plane by 90°. Note that these 90° variations were also tested for the wall example, but not

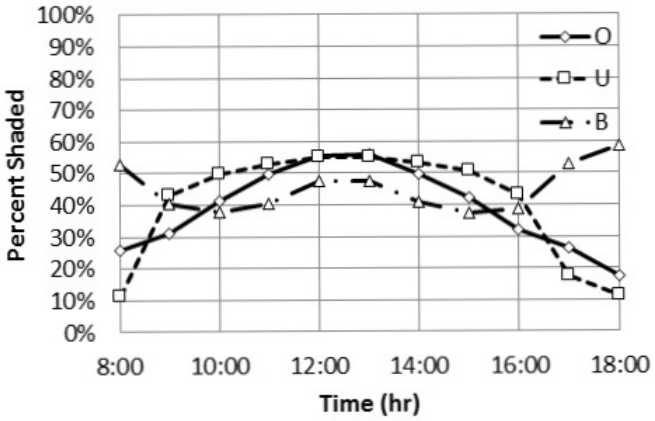

Figure 2.12: Percent of the surface that is self-shaded with respect to time of day for the overhang shape with period of $0.500m$ (O), the unidirectional shape with period of $0.125m$ (U), and the bidirectional shape with period of $0.125m$ (B), all with the original orientation.

shown/discussed previously since they were all considerably less effective in self-shading the surfaces compared to the original orientations (which is a relatively intuitive result based on the expected path of the sun with respect to a West facing vertical surface).

Figure 2.12 shows the percentage of self-shading with respect to time for the optimal variation (i.e., period value and rotation producing the highest total shading) of the three basic shapes on the roof façade. There are significant differences between the self-shading provided by each shape (and parameter variation) for the roof example compared to the wall. First, while the period of 0.125 m provided the most self-shading for all shapes on the wall, the period of 0.500 m provided the most self-shading for the overhang shape on the roof. In addition, the change in the percent shading over time for each shape (i.e., the shading curve) is substantially different for the roof compared to the wall, with the beginning of the day having considerably more differences between the shapes for the roof case. Also of note is the fact that the original orientations overall provided higher shading compared to their 90° rotation counterparts, but the 90° rotations provided the highest self-shading at specific hours. In particular, the bidirectional sin-wave shape had the highest amount of self-shading at both the beginning and end of the day for the roof, when considering no rotation, but never had the highest self shading for the vertical wall. The total percent surface-hours of shade was also much higher for

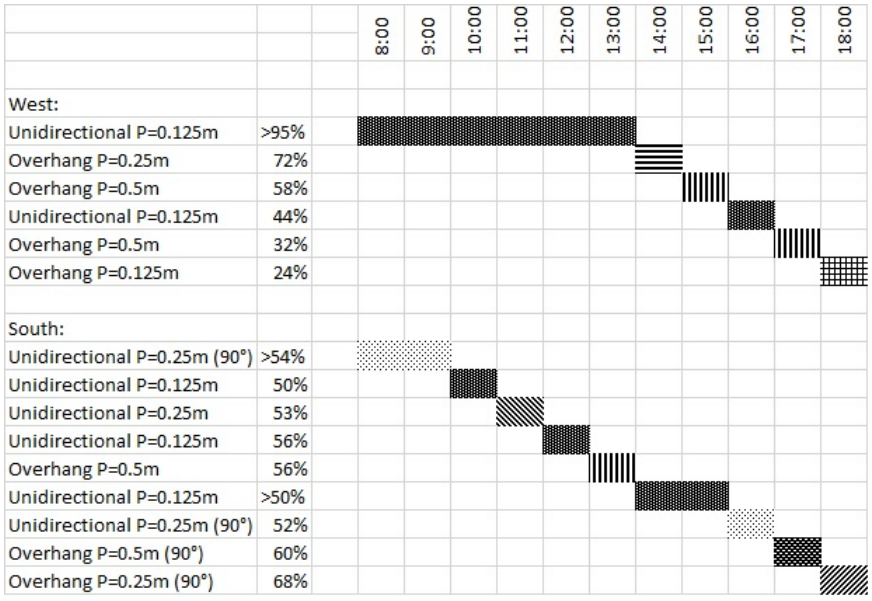

Figure 2.13: Gantt chart representing the shape sequences for the West wall and South roof façades that maximize the total self-shading over the day.

the bidirectional sin-wave shape, indicating that it provides a higher shading on average.

To further compare the two building locations, Figure 2.13 shows the combination of the shapes that maximizes the total shaded area over the day by allowing the tile shape to change every hour (not considering the cost of the shape changes) for the roof example compared to the analogous combination previously shown for the wall example. In particular, the optimal combination for the roof was considerably more dynamic, with eight shape changes between seven shape variations, which is a change almost every hour, compared to just five changes between five variations for the wall (which is due to the West wall being shaded by the building at the beginning of the day). In addition, maximizing the self-shading through morphing had a significantly larger effect on the roof, with the optimized shape change sequence yielding 5.47 total percent surface-hours of shade, which is 24.6% greater than the highest value for any of the static shapes, compared to the 4.5% increase provided by morphing for the wall. As a reminder, this study solely considered the increase in shaded area, no consideration was given to solar irradiance. It should be noted that even though the bidirectional sin-wave was the best static shape in terms of total percent surface-hours of shade, it never provided the highest self-shading of all variations considered at any specific hour, so

it does not appear in Figure 2.13. If there was a limitation on the number of morphs, the bidirectional sin-wave would most likely be in the optimal scheme.

2.5 Conclusions and Future Directions

A concept was presented and numerically investigated for a morphing building tile that would reduce solar irradiance entering buildings by changing the surface topography so that the building envelope is self-shading, thereby reducing energy used by internal temperature control. Numerical case studies were used to evaluate the capabilities of this concept with three basic wrinkle patterns, both static and dynamically changing, to self-shade a building surface over the course of a day. The results indicated that a morphing surface can provide an increase in total percent surface-hours of shade as large as 24.6%, in comparison to the highest performing static (non-morphing) shapes. However, it was noted that there is an expected tradeoff in the mechanical cost to change the surface topography. For example, it is expected that there will be a point in the design where the increase in self-shading from further morphing will not be worth the energy required to achieve morphing (e.g., through material activation and/or mechanical actuation if using a smart material component). In particular, the results showed a substantial reduction in the improvement to the self-shading after three shape changes for the designs considered. Yet, a significant change in self-shading behavior depending upon the tile location was observed, in terms of both total shading capability and the benefits of morphing. Therefore, separate design optimizations, such as that presented, would likely be beneficial for tiles that would be located in different geographic locations and positions/orientations on the building surface.

Although the results presented show promise for a morphing self-shading tile technology to significantly improve solar interaction for a building envelope, there are several considerations moving forward with development. One critical consideration is the full effect that this technology will have on the energy demand of a building. Currently it is assumed the change in shaded surface area directly affects the solar gains, with no consideration of other physical factors such as changes in either conductive or convective heat flow related to the change in

shape. This physical process needs further investigation to truly understand the potential of the technology proposed herein and those that are similar. Another consideration is the choice/development of a smart material solution out of the multitude of existing concepts to facilitate the controllable surface topography. For example, two smart materials that are potentially applicable are shape memory alloys (SMAs) [52–55] and shape memory polymers [51, 56–58]. Both SMAs and SMPs could aid in achieving different tile configurations with a reduced actuation requirement due to the shape memory effect. Additionally, SMPs allow for large strain, which is expected to be a requirement of this morphing tile concept. Another consideration is that throughout the presented work the design only considered a finite number of tile topographies. As such, future work to explore not only optimization of the morphing scheme, but also the surface topography of the tile could lead to improvements to both efficiency and effectiveness.

3.0 Computational Design Optimization of a Smart Material Shape Changing Building Skin Tile

3.1 Overview

The development and evaluation of a computational approach for optimal design of a smart material shape changing building skin is presented and numerically evaluated. Specifically, a unique shape-based approach is utilized to create an optimization approach to identify the activation and actuation mechanisms to minimize the difference between a desired shape and the estimated morphed shape. Three potential metrics of shape difference are considered and their capability to facilitate an efficient optimization process leading to accurate shape matching is evaluated. Details of the optimal design framework are presented, particularly focusing on the shape difference metrics as well as the strategy to parameterize the activation of the smart material. In particular, the parameterization strategy is a unique approach to easily integrate controllable localized activation within a smart material structure in a generally applicable way that does not limit the design search space. A series of numerical design examples are presented based on the concept of a smart material (e.g., shape memory polymer) shape changing tile that can be activated and actuated in a variety of ways to achieve desirable surface wrinkle patterns. Results indicate that the shape-based approach can consistently determine the mechanisms of morphing needed to accurately match a target shape. Furthermore, it is shown that localized material activation can lead to not only a more accurate shape but also requires less energy and actuation devices to do so.

3.2 Introduction

Responsive building skins have been shown to have effects on all the main energy consumers of commercial buildings: lighting, ventilation, and heating and cooling [59]. Examples include the skin used on the Media-TIC building [32], which uses a light sensor to measure

thermal loads on a building and inflates portions of the skin in order to increase insulation during times of high thermal loading, and the Heliotrace system [32] and the responsive skin of the Al Bahar towers [34], which both utilize a series of mechanical apertures that open or close portions of the skin, allowing different amounts of light to enter the building. In most cases the current technologies are binary, either activated or inactivated based on a stimulus threshold, or have a limited number of configurations. Thus, significant work still remains to achieve technologies that can adapt to multiple environmental states and have a higher level of customization. One possibility proposed to increase functionality of responsive building façade is the integration of smart materials [51, 55, 60, 61].

A recent example of a smart material morphing structure with applications to building skins/facades involves the use of hygromorphic materials that simulate the opening and closing of conifer cones [39]. In this recent application, a shape changing surface tile is created by combining a hygromorphic layer with a passive (non-smart material) layer. The hygromorphic layer has a larger coefficient of hygroexpansion than the passive layer, therefore, the growth or shrinkage of the hygromorphic layer will be larger as well. This results in the tile either curling outwards or inwards (opening or closing) based on moisture levels of the environment. Currently this hygromorphic application is focused on architectural aesthetics and psychological benefits to occupants. Alternatively, Barrett et al. developed an adaptive material building skin called "Thermadapt" that uses bimetal sheet layers to change shape based on external thermal loading [35]. In a similar way to the hygromorphic example, the Thermadapt concept uses differences in coefficients of expansion to create motion, but through thermal excitation rather than moisture. However, the application of Thermadapt has been focused specifically on increasing or decreasing the shading on a building surface to affect solar irradiation heating. In this case, the Thermadapt composite would have an outer layer with a lower coefficient of thermal expansion than the inner layer. Therefore, when the temperature rises the inner layer expands more than the outer layer causing the covering to curve outwards into a shading configuration. During periods of lower temperature, the opposite occurs and the inner layer contracts more than the outer layer causing the covering to curve inwards forming an air pocket that helps insulate the building.

The technologies being developed for shape changing building skins that use smart materials have primarily relied upon passive mechanisms, in that the shape change that occurs is caused by the material being activated by changes in the surrounding environmental conditions (e.g., moisture change [39] or temperature change [35]). Passive use of the smart material has the benefit of not requiring any additional intervention or energy costs to the user beyond maintenance requirements. Yet, passive use of the material may limit the extent that the behavior of the structure can be customized and may limit feasibility of certain applications or material types if the activating environmental condition does not correlate with the desired material change. Alternatively, active use of smart materials for shape changing structures that include a mechanism to apply activation energy and/or actuation to the structure have the obvious disadvantage of energy consumption, but can substantially increase the range of potential shape changes and the potential applications of the technology overall. There have been several application areas of smart material structures where this benefit of active use has outweighed the additional energy costs, such as morphing aircraft applications [56, 62, 63]. Although active use of smart materials for shape changing structures can significantly expand the potential functions of the structure, this expansion can also substantially increase the initial challenge of designing the smart material structure.

With any degree of complexity in the desired behavior, the active use of smart materials for shape changing structures can include nearly infinite non-trivial potential design solutions, when potentially seeking to define localized stimulation/activation, a multitude of mechanical actuation methods, or even the use of multiple smart materials together. Such design problems are often best handled through a computational optimal design approach, which have already been used for several smart material structure design applications [56, 62–70]. Computational approaches are particularly beneficial for problems that have non-trivial and/or non-intuitive solutions, and complex objectives and constraints. Although substantial work has been done developing computational design methods for various applications, with any new application there are new and unique challenges, ranging from the definition of the forward model and its parameterization to the quantification of the design objective and constraints.

The current study presents a computational framework for the design of the active mechanisms for a smart material building skin tile to optimally achieve a desired shape change. The target of shape change is chosen as it aligns with the prior work using hygromorphic structures, which was noted to be largely for aesthetic reasons thus far [71], while also allowing for inclusion of other more functional objectives, such as increasing shading similar to the "Thermadapt" case [35]. In other words, it is assumed that some prior analysis to define the desired combination of appearance and function has been performed to provide the target shape change to be designed toward. As such, one particular focus of the study is on determining an appropriate objective function that quantifies the difference between the desired shape change and the shape change predicted by the forward model for the optimization procedure. In addition, focus is also placed on the strategy to define the unknown design parameters, particularly to ensure the localized activation is feasible to implement without sacrificing the shape change capability. Although more generally applicable, the design strategy is presented in the context of an example design of the mechanical actuation and material activation of tile entirely comprised of a homogeneous smart material. In the following section, the details of this exemplar smart material shape changing building skin tile are provided. In Section 3 the general computational inverse problem for the design of a smart material building skin tile is presented. Numerical examples, their results, and discussion are then given in Section 4, which is followed by concluding remarks in Section 5.

3.3 Design Concept

The design concept considered herein is an adaptive shape changing "wrinkled" surface tile based upon the prior work developing building surface "cactus tiles" by Clifford [41]. The original cactus tile objective was to have static "wrinkled" surface tiles that were both aesthetically pleasing and had functional benefits in terms of self-shading. However, it is envisioned that adding the capability of such tiles to change between wrinkle patterns, would further enhance the original benefits and potentially include many other functional behaviors [41, 72, 73]. As shown in Figure 3.1, the proposed mechanism to produce a tile that can

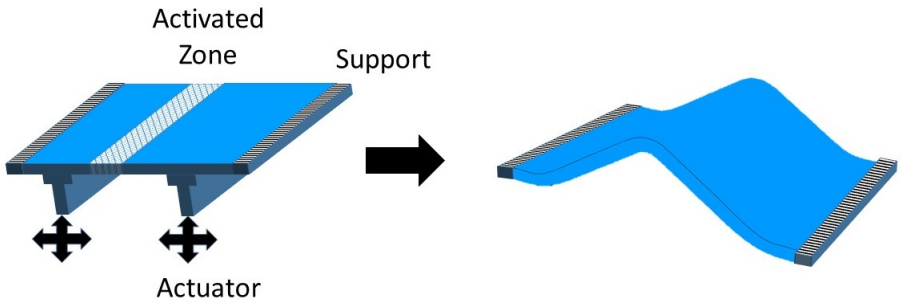

Figure 3.1: Concept of a smart material being activated and mechanically actuated.

morph between different wrinkle patterns (i.e., shape changing cactus tile) is envisioned to be controllable activation of the smart material comprising the tile (e.g., softening) and mechanical actuation to deform the tile into a desired shape. For the sake of simplicity, this work does not consider the activation process (e.g., heat transfer process if thermal activation was used) and assumes that the deformed shape could be perfectly "locked in" once activation is removed. However, these behaviors could be included in the forward modeling in subsequent work without significant change to the computational design strategy. Similarly, the overall dimensions of the tile were assumed to be given/fixed. Thus, the remaining unknown variables to determine for the design of this tile concept are the locations and magnitude of mechanical actuation (i.e., applied force and/or displacement) and the location and size of the regions of the material to be activated.

3.4 Design Solution Strategy

The design strategy considered herein is based on utilizing non-linear optimization in combination with a numerical representation of the shape changing tile to be designed. As noted, the primary objective of the optimal design is to achieve a given desired shape change. In this work, the target shape was assumed to be defined as the desired outer surface shape of the tile. However, as is often the case with smart material applications, minimizing the energy cost of the shape changing process was also considered as an objective of the design. Thus, the design problem can be written in the general form of the following constrained

optimization problem:

$$\begin{aligned} \underset{\vec{\gamma}}{\text{minimize:}} \quad & \left\{C\left(S_T, S_F(\vec{u})\right), E(\vec{u}, \vec{\gamma})\right\} \\ \text{subject to:} \quad & F(\vec{u}, \vec{\gamma}) = 0 \\ & \vec{b}_l \leq A(\vec{\gamma}) \leq \vec{b}_u, \end{aligned} \tag{3.1}$$

where S_T is the target surface shape, S_F is the predicted morphed shape of tile as defined by the deformation of the tile, $\vec{u}$, estimated by the solution of the forward problem, $F(\vec{u}, \vec{\gamma}) = 0$ (i.e., the partial differential equation constraint), for a given set of actuation and activation design parameters, $\vec{\gamma}$, $C(\cdot, \cdot)$ is the metric that quantifies the difference between two shapes, $E(\vec{u}, \vec{\gamma})$ is the estimated energy consumption required to complete the shape change process, $\vec{b}_l$ and $\vec{b}_u$ are the lower and upper bound constraint vectors, respectively, and $A(\vec{\gamma})$ is the operator that forms the necessary constraint equations involving the design parameters. Note that this is the general form of the optimization problem considered herein, and the examples will more specifically state the respective components, including the example-specific objective functions, design parameters, and constraints utilized.

An estimate of the optimal design solution can be found through any preferred optimization strategy applied to Equation 3.1 to determine the actuation and activation parameters (within the physical bounds) that minimizes the difference between the deformed tile shape predicted by the forward problem and the target shape. Both standard gradient-based and non-gradient-based optimization strategies were utilized in the present study, with specific details provided in the Examples Section. As noted, specific focuses of the development were the shape difference metric and the parameterization strategy, which are discussed in more detail in the following.

3.4.1 Shape Difference Metric

There are multiple methods of shape description that can be used to quantify the difference between two shapes. In general, shape descriptors are separated into two categories: region-based shape descriptors [74–76], which calculate the descriptor based on the entire volume of a shape, and contour-based shape descriptors [76], which calculate the descriptor based solely on the contour (or boundary) of the shape. Generally, region-based shape

descriptors are not well suited for this type of application and so only contour-based descriptors were considered. Specifically, a sub-category of contour-based shape descriptors, correspondence-based shape descriptors, were considered.

One relatively intuitive correspondence-based approach is to project the target shape onto the initial tile shape (i.e., flat tile) to establish a point-to-point correspondence, and then measure the difference between the location of the surface points on the target shape and the deformed location of the surface points estimated for a given design solution for all of these now corresponding points. Specifically for this work, a projection-based metric for a discretized tile surface was defined as:

$$PM_d = \sum_{i=1}^{N_C} \parallel \vec{x}_{Si} - \vec{x}_{Fi} \parallel, \tag{3.2}$$

where $\vec{x}_{Si}$ and $\vec{x}_{Fi}$ are the spatial coordinates on the target shape and deformed tile shape from the design estimate, respectively, for the i^{th} point in the correspondence set, N_C is the number of points in the point-to-point correspondence, and $\parallel \cdot \parallel$ is the Euclidean distance. Other similar approaches that first form a set of corresponding points between a target shape and an estimated morphed structure shape have been used in similar design applications [66]. However, these approaches can potentially limit the design space as they conceptually change the design problem to matching a desired displacement of certain points rather than a more general shape. Furthermore, the projection strategy considered here to form the correspondence is only applicable to target shapes with non-overlapping regions so that a one-to-one correspondence is formed. Alternatively, the Hausdorff distance and similar variants have been developed to quantify the difference between two shapes in a more general sense and with no limitation on the type of shapes being compared [76, 77].

Assuming the shapes are discretized, the Hausdorff distance is a point-to-point matching that finds the maximum closest pairing between all the points on each shape. The Hausdorff distance between two shapes discretized into two collections of points S_1 and S_2 is defined as:

$$H_d(S_1, S_2) = \max(D(S_1, S_2), D(S_2, S_1)), \tag{3.3}$$

$$\text{where: } D(S_1, S_2) = \max_{\vec{x}_1 \in S_1} \min_{\vec{x}_2 \in S_2} \parallel \vec{x}_1 - \vec{x}_2 \parallel, \tag{3.4}$$

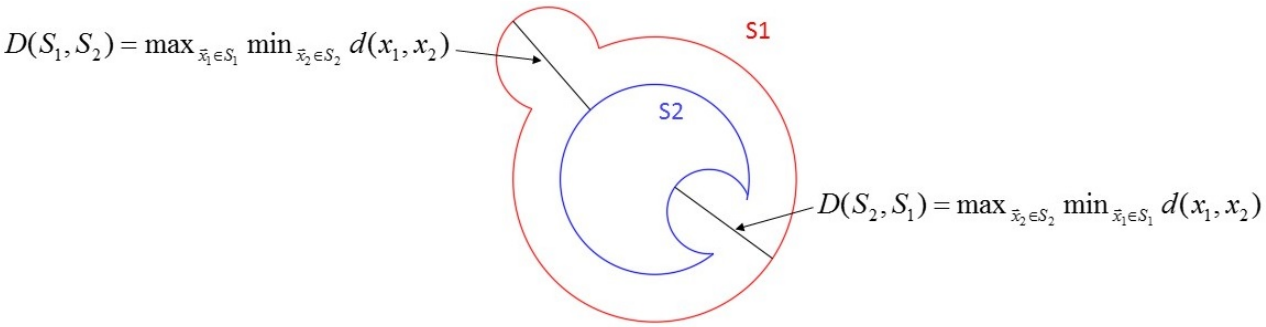

Figure 3.2: Representation of the distances $D(S_1, S_2)$ and $D(S_2, S_1)$ used in Equation 3.4 for shapes S_1 and S_2

$\vec{x}_1$ is the collection of points in shape S_1, $\vec{x}_2$ is the collection of point in shape S_2, and again $\| \cdot \|$ is the Euclidean distance. A visual representation of $D(S_1, S_2)$ and $D(S_1, S_2)$ can be seen in Figure 3.2. An important note is that this Standard Hausdorff distance defined by Equation 3.3 can suffer from over-sensitivity to outliers, which can be expected as the Hausdorff distance is analogous to a L_∞ norm. To address these issues with the Hausdorff distance several modified versions have been developed and explored [78]. For the present study the best performing modification in [78] was also considered alongside the Standard Hausdorff distance and the projection-based distance which can be defined as:

$$MH_d(S_1, S_2) = \max(M(S_1, S_2), M(S_2, S_1)) \tag{3.5}$$

$$\text{where: } M(S_1, S_2) = \frac{1}{N_1} \sum_{i=1}^{N_1} \min_{\vec{x}_2 \in S_2} \| \vec{x}_1 i - \vec{x}_2 \|, \tag{3.6}$$

N_1 is the number of points on shape S_1, $\vec{x}_1 i$ is the i^{th} point in $\vec{x}_1$, and N_2 is the number of points on shape S_2. This Modified Hausdorff distance is analogous to an L_1 norm and ensures that every point on each shape contributes to the distance metric.

3.4.2 Actuation and Activation Parameterization

When considering a smart material structure such as the proposed SMP building tile, there are many methods available to activate and actuate the structure to achieve the desired

behavior. Generally, in similar applications the entirety of the smart material is activated. However, additional functionality can be achieved through a mixture of smart material and a passive material, such as in [79] which considered a Shape Memory Alloy (SMA) mesh binded to a passive material to achieve a self-folding structure. Alternatively, others have considered partial (or localized) smart material activation to increase functionality [70]. As the activation process was not included in the system model for the work herein, there is no difference conceptually in the optimal design procedure whether the intention is to use localized activation or to combine active and passive materials. In both cases, the objective of the activation portion of the optimal design are the same, which is to define the distribution (i.e., size and location) of the regions of the structure that would have the activated (i.e., soft) material properties.

For any inverse problem where the objective is to obtain the material property distribution, there are many different ways to parameterize the unknowns. The main concern with the parameterization is often the trade-off between generality (i.e., being able to capture any possible distribution) and computational expense. The more general the parameterization the higher the computational expense of the problem. For example, finite element-type discretizations of a material property distribution [80], for which every node or element of a mesh can have a different property, have a high degree of general applicability. However, the large number of unknowns in a mesh description can substantially increase computational expense and may require some kind of regularization or other additional consideration to address ill-posedness. Alternatively, many lower-dimensional parameterizations have been considered to reduce computational expense and avoid ill-posedness, such as the use of radial basis functions [81]. The challenge with lowering the dimension of the parameterization is that it is often problem-dependent and best used when some *a priori* information is available or can be estimated regarding the expected type of spatial distribution.

In order to balance computational cost with generality for this specific application, the distribution of activated material was parameterized into a fixed number of activated regions, assuming the material would be activated uniformly through the thickness. The number of regions was chosen to be sufficiently large to allow for complex solutions (e.g., many disconnected activated regions), but the regions could overlap to allow for simple solutions as well (e.g., a single local activated region). Furthermore, a threshold was set so that any small gaps between activated or inactivated material regions would be removed to improve practicality of the design solutions. Thus, the material distribution was defined by m discrete activated material sections centered at variable planar locations, $\{d_j\}_{j=1}^{m}$, along the tile with variable widths/diameters, $\{l_j\}_{j=1}^{m}$. An important note is that this parameterization of the material activation is expected to lead to non-unique solutions in terms of the parameters, even for cases where there is one optimal distribution of material properties. However, this non-uniqueness was not a concern, since the distribution and not the parameters themselves is the important outcome, and uniqueness in optimal design problems is generally not critical. The actuation was chosen to be implemented through variable applied pressure and a series of n discrete actuators at variable planar locations, $\{c_i\}_{i=1}^{n}$, and with variable horizontal and vertical prescribed displacements, $\{u_i\}_{i=1}^{n}$ and $\{w_i\}_{i=1}^{n}$, respectively. Figure 3.3 shows a two-dimensional (2D) schematic of the tile with an applied pressure P, n discrete actuators, and m discrete activated zones for a maximum of $3n + 2m + 1$ potential design variables to be determined.

3.5 Results and Discussion

Several numerical case studies of the design of a smart material shape changing tile were considered to evaluate the capability of the shape-based optimal design strategy presented to achieve suitable design solutions and examine any potential benefits or limitations for the various component options discussed. In all examples the conceptual shape-changing tile was taken to be 10.16 *cm*-by-10.16 *cm* (4 *in*-by-4 *in*) with a thickness of 0.25 *cm* (0.1 *in*) and the activated and inactivated mechanical material properties were based upon those for a stan-

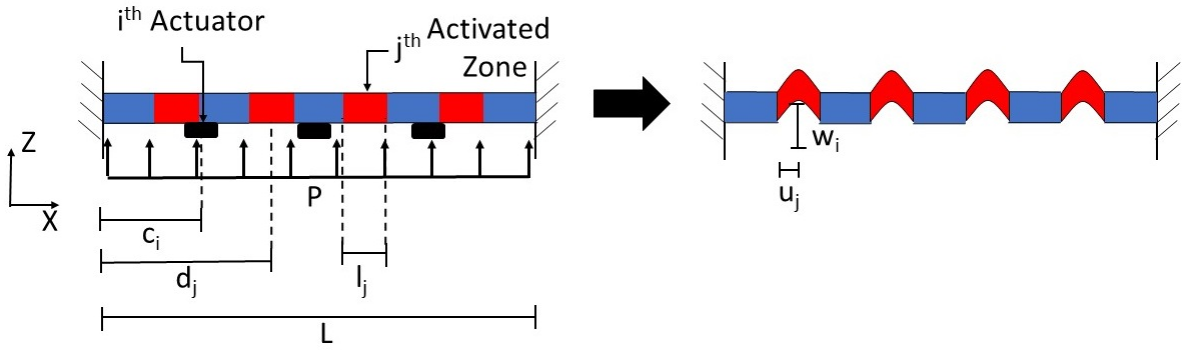

Figure 3.3: Schematic of the tile concept in which applied pressure (P), a series of n discrete actuators at variable locations, and a set of m activation patches (red) at variable locations are used to deform the tile to achieve a given target shape.

dard shape memory polymer (SMP) [82]. Although it is not expected that such a material would be suitable for architectural applications without further development/modification, the shape memory and large recoverable strain capabilities of SMP [83] would be significantly beneficial for the proposed concept of a shape changing building skin tile. Therefore, SMP was chosen as the exemplar smart material for the development of this concept. The material was assumed to be an isotropic Neo-Hookean hyperelastic material with activated and inactivated Young's moduli of 2.4 MPa and 1034 MPa, respectively, and a constant Poisson's ratio of 0.45. The process to change the shape (i.e., deform) the tile was assumed to be quasi-static. As previously noted, the material was assumed to be activated instantaneously so that regions of the tile were either activated or inactivated completely, and it was further assumed that all activation of material occurred prior to the application of any actuation. A final important consideration not yet mentioned for the design of this type of smart material shape-changing structure is to ensure that the design solution does not damage the structure. Although a constraint could be included in the design optimization problem to prevent solutions that damage the material [70], preliminary tests showed this to be unnecessary for the case studies considered. However, the final design solutions were

still checked to ensure no damage of the material would occur by confirming the maximum principal strain did not exceed damage limits anywhere of 30% for inactivated material or 400% for activated material.

The numerical case studies were broken into three groups to evaluate different components of the design solution strategy with the first two groups considering a 2D system, while the third group extended to a three-dimensional (3D) system. In the first group of case studies the capability of the correspondence-based shape difference metrics as objective functions to accurately match a target shape were investigated. For this first group of tests, the tile was assumed to be fully activated (i.e., the only optimization parameters to be considered were the mechanical actuation variables) to simplify the design solution space, so that the capability of the various objective functions could be more easily compared. Full activation was considered to focus on the design objective functions, rather than comparing the capabilities of local to global activation. Furthermore, energy cost was ignored for these first tests (i.e., not included in the optimization), in order to directly determine the accuracy of the correspondence-based metrics as objective functions. These cases examining the shape matching capability were further divided into two groups of tests: (1) evaluation of example target shapes that have a one-to-one vertical projection onto a flat tile and (2) evaluation of example target shapes that do not have a one-to-one vertical projection onto a flat tile. After establishing the preferred shape difference metric, the second group of case studies focused on the use of localized material activation for the design of a smart material shape-changing structure. This second group of case studies was also broken into two groups of tests: (1) a comparison of the shape matching accuracy with full activation to the shape matching accuracy with localized activation and (2) analysis of the trade-off between shape matching accuracy and the energy cost to perform the shape change. Additionally, to have some consistency between all of the examples for these first two groups of tests, all target shapes were set to have a total surface area of 150% of the original flat tile surface area (i.e., 103.23 cm^2). The final numerical case study investigated the generalization of the design optimization strategy by considering a 3D target tile shape, as well as variations in the tile support conditions and methods of activation and actuation.

3.5.1 Capability of a Shape-Based Objectives for Optimal Design

For both subgroups of these first numerical case studies, a constrained gradient-based interior point algorithm (fmincon in MATLAB [84]) was used to solve Equation 3.1 by minimizing $C\left(S_T, S_F(\vec{u})\right)$ (removing the energy term from Equation 3.1). For each numerical example, the gradient-based optimization was repeated with 10 randomly generated initial guesses and the solution was taken to be the result with the lowest respective objective function value. The optimization stopping criteria was set to be when the the change in objective function between iterations fell below the tolerance value of 10^{-6}. Starting with one actuator, the number of actuators for the design was increased by one and the optimization repeated until the shape matching capability did not noticeably improve (i.e., convergence was achieved in terms of the number of actuators). This type of optimization was done for simplicity since the parameter for the number of actuators is an integer, while the remaining design parameters are continuous real numbers. Each of the correspondence-based objective functions defined in Section 3.4.1, the Standard Hausdorff distance, the Modified Hausdorff distance, and the projection-based distance, were used in turn as the objective function for the optimization process. In order to have a fair comparison between each of the potential design solutions, regardless of the objective function used in the optimization process, the Standard Hausdorff distance and Modified Hausdorff distance were calculated for the final designed tile shapes in comparison to the target shapes. The design problem was constrained to be two-dimensional by assuming both the activation and actuation would be constant in one planar direction. Additionally, for this first group of numerical cases the two end faces of the tile that were parallel to the direction of constant activation and actuation were taken to be fixed with zero displacement in all directions (as shown in Figure 3.3), while all other faces were free to deform due to the actuation detailed in Section 3.4.2.

3.5.1.1 Target Shapes with a One-to-One Vertical Projection Figure 3.4 shows the two target shapes with a one-to-one vertical projection, an "overhang" shape (Target Shape 1) and a unidirectional sin-wave (Target Shape 2). Both shapes were based upon work in [73], which detailed the self-shading performance of these shapes in a similar application

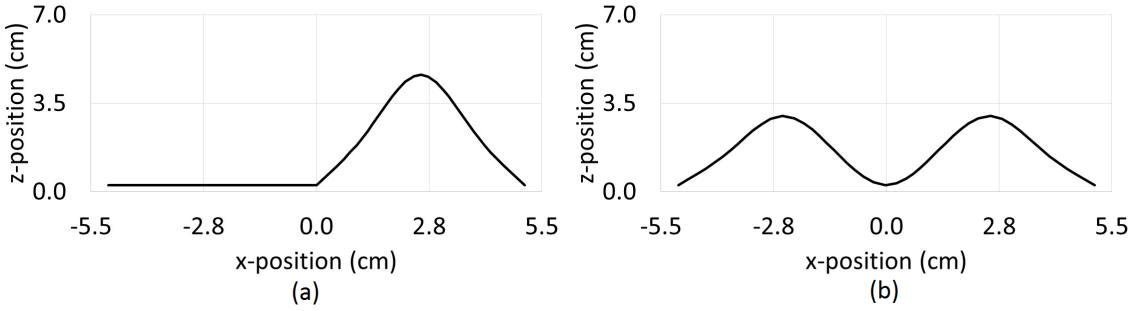

Figure 3.4: The two target shapes considered in the uniquely projected group. (a) An "overhang" shape (Target Shape 1) and (b) a unidirectional sin-wave (Target Shape 2).

for a building skin. Target Shape 1 had a flat (i.e., undeformed) cross-section for half of the tile, and the other half had a cross-section defined by a single sin wave with amplitude 4.57 cm and a period of 5.08 cm. Target Shape 2 was defined by a sin wave cross-section with amplitude 2.74 cm and a period of 5.08 cm.

Figure 3.5 shows the Standard and Modified Hausdorff distances for the final design shapes obtained from optimizing with respect to each of the correspondence-based objective functions with one through five discrete actuators for Target Shapes 1. No sufficiently accurate solution could be found for a one actuator design, which is consistent with intuition. However, all design solutions that utilized two or more actuators for Target Shape 1 resulted in Standard and Modified Hausdorff distances less than 10% the length increase (2.08 cm) of the tile, with only the exception of the four actuator case using the Standard Hausdorff objective function that had a slightly higher error. In other words, the design solution converged at two actuators for Target Shape 1. The shape matching for Target Shape 1 when minimizing with respect to all three objective functions can be seen in Figure 3.6, which shows the final deformed shape and the design solution (i.e., actuator placement and pressure) corresponding to each objective function. Clearly, designs that can accurately match the target shape were able to be obtained when they existed, regardless of the specific shape-based objective function utilized in this case. The convergence at two actuators is expected based on the key features of the shape (i.e., one actuator to hold the first half of the tile in place and a second actuator to define the height of the "overhang"). Also of note, there are fluctuations in the Standard and Modified Hausdorff distances for the final design shapes,

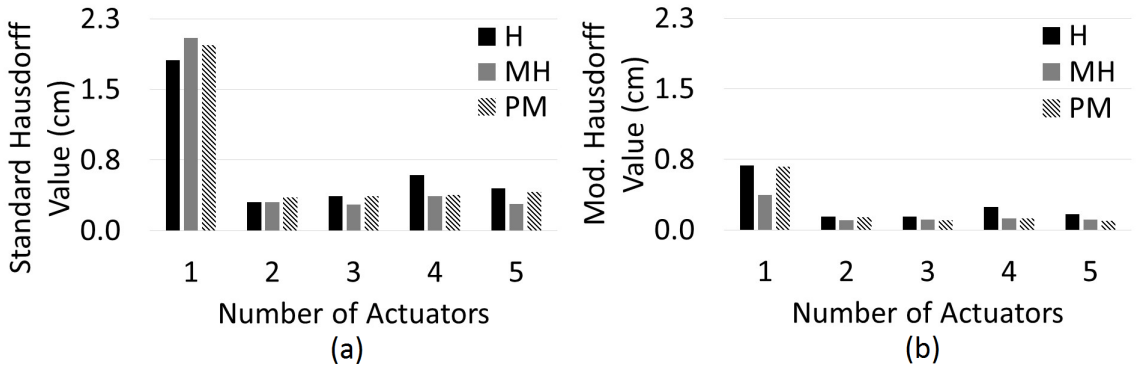

Figure 3.5: (a) Standard Hausdorff distance value and (b) Modified Hausdorff distance for optimal designs using various numbers of actuators for design solutions minimizing with respect to the Standard Hausdorff, Modified Hausdorff, and projection-based distances for Target Shape 1.

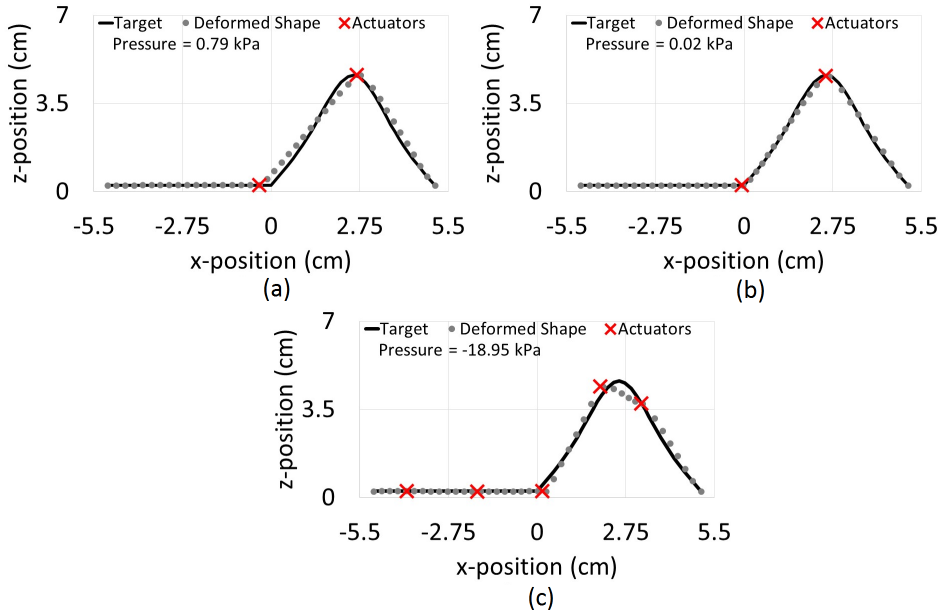

Figure 3.6: The morphed tile shape for the "best" design solution, target shape, and actuator placement for the optimization using (a) the Standard Hausdorff distance, (b) the Modified Hausdorff distance, and (c) the projection-based distance for Target Shape 1.

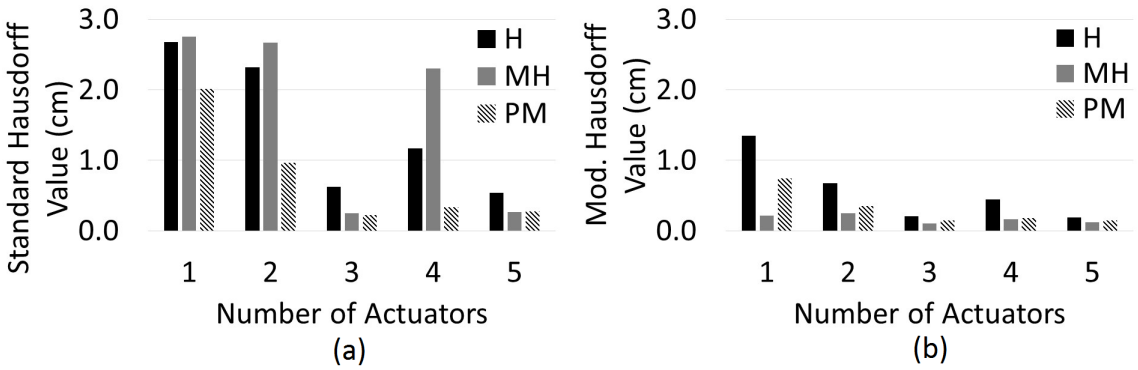

Figure 3.7: (a) Standard Hausdorff distance value and (b) Modified Hausdorff distance for optimal designs using various numbers of actuators for design solutions minimizing with respect to the Standard Hausdorff, Modified Hausdorff, and projection-based distances for Target Shape 2.

most notably for the solutions obtained by minimizing the Standard Hausdorff distance. The larger fluctuations in the solutions, imply that the Standard Hausdorff Distance creates a more complex solution space that is more difficult for an optimization algorithm to traverse (i.e., more local minima exist in comparison to the other objective functions).

The results for Target Shape 2 were similar to those for Target Shape 1, but accurate design solutions were not able to be obtained until at least 3 actuators were utilized (Figure 3.7). The shape matching for Target Shape 2 when minimizing with respect to all three objective functions can be seen in Figure 3.8, which shows the final deformed shape and the design solution corresponding to each objective function. A main difference in the results for Target Shape 2 is that an odd number of actuators were necessary to accurately match the desired shape, with even numbers of actuators resulting in errors as high as 300% more than when using an odd number of actuators. This is due to the need for an odd number of actuators to be able to match the key features of a symmetric shape, by placing one actuator at the line of symmetry and an equal number on each side of the line of symmetry. Consistent with the results from Target Shape 1, the Standard Hausdorff distance objective function resulted in a more challenging optimization problem and led to the identification of inaccurate design solutions in terms of the shape matching for some cases of Target Shape

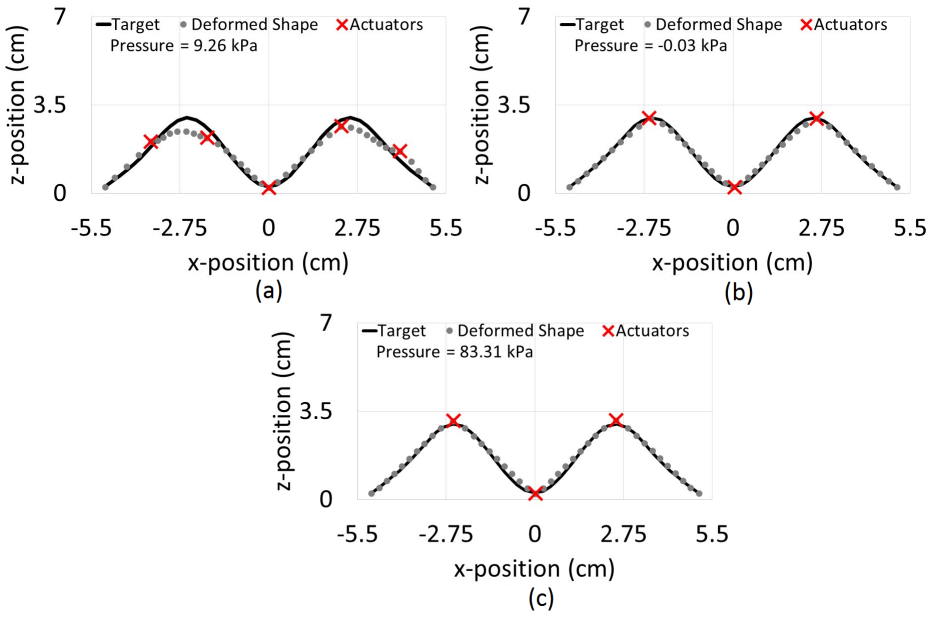

Figure 3.8: The morphed tile shape for the "best" design solution, target shape, and actuator placement for the optimization using (a) the Standard Hausdorff distance, (b) the Modified Hausdorff distance, and (c) the projection-based distance for Target Shape 2.

2.

An important note is there are design solutions that have nearly identical actuator placements and deformations, but substantially different applied pressure values for both Target Shapes 1 and 2, as seen in Figures 3.6 and 3.8. This could be interpreted as the pressure variable being a superfluous variable in the design of the shape changing mechanisms and should likely be removed from the system if implemented for these cases. However, as will be shown in the following, the ability to control an applied pressure became significant for more complicated target shapes and when utilizing localized activation.

3.5.1.2 Target Shapes without a One-to-One Vertical Projection As projection is not applicable for these shapes, only the Standard and Modified Hausdorff distances were used as objective functions within the design optimization procedure for this set of tests. Additionally, in these examples the number of actuators was incremented from one to seven, due to the increased target shape complexity. Figure 3.9 shows the two target shapes without

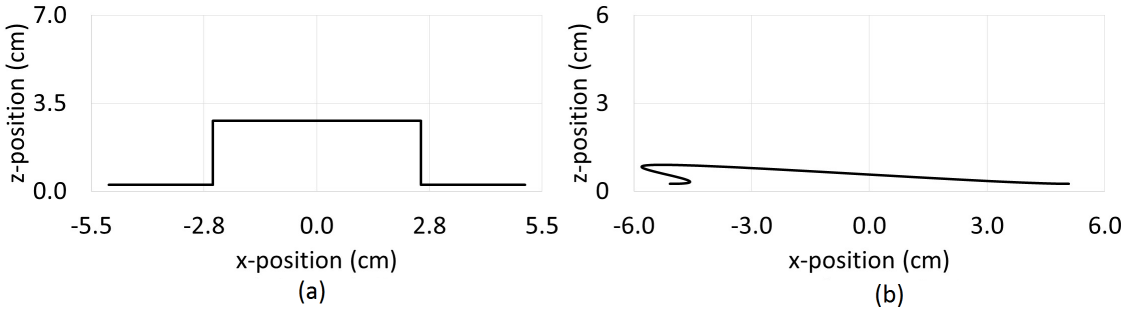

Figure 3.9: The two target shapes considered in the non-uniquely projected group. (a) A boxcar function (Target Shape 3) and (b) a distorted sin-wave (Target Shape 4).

a one-to-one vertical projection, a boxcar function (Target Shape 3) and a distorted sin-wave (Target Shape 4). Target Shape 3 was a centered boxcar function with a width of 5.08 *cm* and a height of 2.54 *cm*. Target Shape 4 was a centered sin-wave with an amplitude of 2.62 *cm* and a period of 10.16 *cm*, which was rotated 75° about the out-of-plane axis. Figures 3.10 and 3.11 show the Standard and Modified Hausdorff distances for the final design shapes obtained from optimizing with respect to those same two applicable correspondence-based objective functions with one through seven discrete actuators for Target Shapes 3 and 4, respectively. Even with the substantial increase in target shape complexity, solutions that clearly matched Target Shapes 3 and 4 could be found. The sufficiency of the design solutions can be visually confirmed through Figures 3.12 and 3.13, which show the final deformed shapes and design solutions corresponding to each objective function. Even though the optimization process typically converged to a design solution with a higher error than the prior set of examples (e.g., error values of approximately 10% of the length change of the tile), the optimization process using the Modified Hausdorff distance led to design solutions that matched both of the complex target shapes accurately. Alternatively, the limitation of the Standard Hausdorff distance that resulted in less consistent optimization was even more significant, with the corresponding design solutions for Target Shapes 3 and 4 being substantially less accurate, both quantitatively and visually.

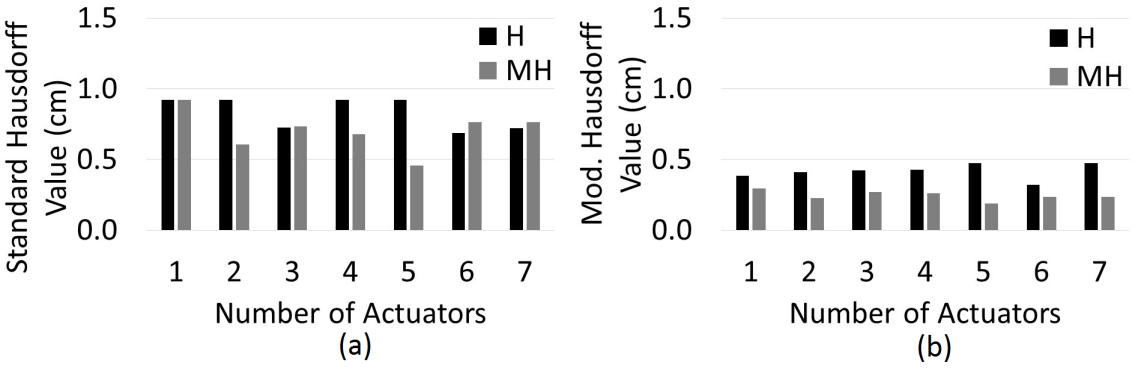

Figure 3.10: (a) Standard Hausdorff distance value and (b) Modified Hausdorff distance for optimal designs using various numbers of actuators for design solutions minimizing with respect to the Standard Hausdorff and Modified Hausdorff distances for Target Shape 3.

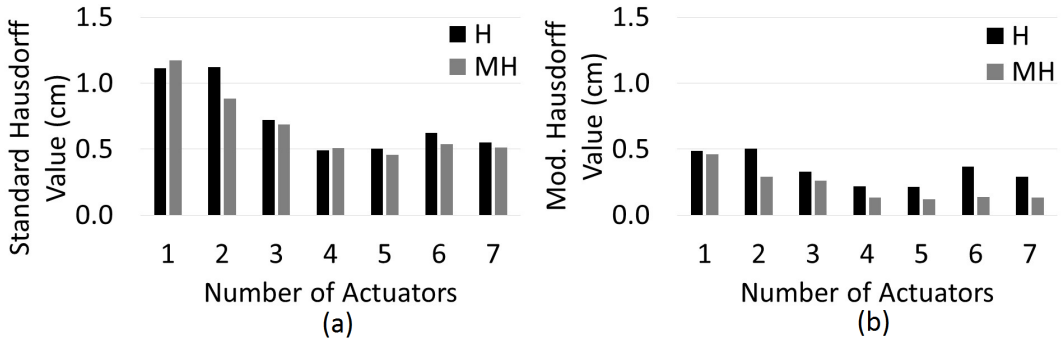

Figure 3.11: (a) Standard Hausdorff distance value and (b) Modified Hausdorff distance for optimal designs using various numbers of actuators for design solutions minimizing with respect to the Standard Hausdorff and Modified Hausdorff distances for Target Shape 4.

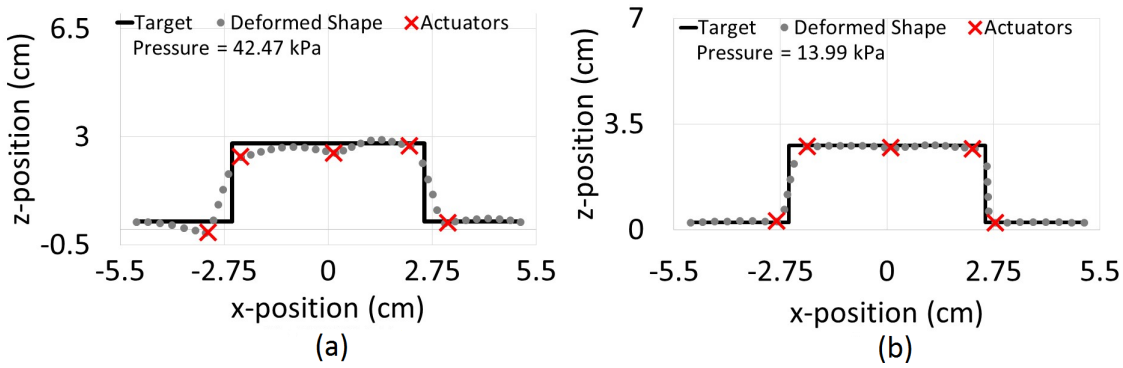

Figure 3.12: The morphed tile shape for the "best" design solution, target shape, and actuator placement for the optimization using (a) the Standard Hausdorff distance and (b) the Modified Hausdorff distance for target shape 3.

Regarding the design variables, as expected the optimal design process revealed that this more complex second set of target shapes required more actuators (four or five) in comparison to the prior example set (two or three actuators) to accurately match the desired shapes. Additionally, in contrast to the previous set of examples, the pressure design variable was an important variable to the design, and consistent pressure values were identified for the design solutions that accurately matched the target shapes.

3.5.2 Locally Activated Shape Changing Tile

When utilizing local activation, the energy cost to change the structures shape varies far more significantly depending upon the design than for the previous cases. Therefore, energy was included as a design objective for all of the following cases, which required the use of multi-objective optimization. In particular, for the remaining tests a controlled, elitist genetic algorithm [85] was used to solve Equation 3.1 by simultaneously minimizing both $C\left(S_T, S_F(\vec{u})\right)$ and $E(\vec{u}, \vec{\gamma})$ to determine potential design solutions. The initial population was set to be 200 and the stopping criteria was set as either a maximum number of generations of $200 * N_D$ (where N_D is the number of design variables) or when the objective function difference between iterations fell below a tolerance of 10^{-4}). The result of the multi-objective optimization for each trial was the Pareto front set of solutions. The Pareto front includes

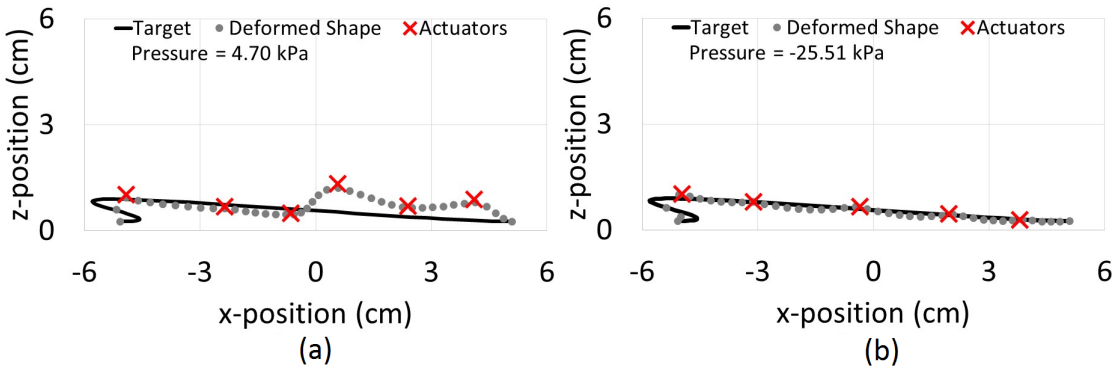

Figure 3.13: The morphed tile shape for the "best" design solution, target shape, and actuator placement for the optimization using (a) the Standard Hausdorff distance and (b) the Modified Hausdorff distance for Target Shape 4.

all of the "best" potential design solutions within the limit of the population size that have a lower value for at least one of the separate objective functions in comparison to any other solution estimate seen throughout the optimization process. This Pareto front is particularly useful to analyze the trade-off between the two objectives, shape matching accuracy and energy cost. Similar to the first group of numerical tests the design problem was again constrained to be 2D and have the same boundary conditions.

As the Modified Hausdorff distance was universally applicable and led to substantially more consistent design solutions compared to the other objectives considered, this was the only shape-based objective function used for the following cases. Based on the example of a thermally activated SMP, the energy required to morph the smart material tile in this application could be quantified from the design pressure, mechanical actuation, and material activation as follows:

$$E = \int_{\Gamma} P(-\vec{n} \cdot \vec{u}) d\Gamma + \sum_{i=1}^{n} \vec{F}_i \vec{u}_i + c_p \rho V_a \Delta T, \tag{3.7}$$

$\vec{n}$ is the unit outward normal to the tile surface where pressure was applied, Γ, $\vec{u}$ is the displacement vector, $\vec{F}_i$ is the resultant force vector needed to displace the i^{th} mechanical actuator by $\vec{u}_i$, c_p is the specific heat of the SMP (taken as $c_p = 2009 \frac{J}{kg-K}$), ρ is the

density of the SMP (taken as $\rho = 35.98\frac{kg}{m^3}$), ΔT is the temperature change required to activate the material, and V_a is the volume of the tile that is activated (determined based on the activated zone parameterization defined in Section 3.4.2). As noted previously, the activation process was not considered within this study. Therefore, to quantify the energy to activate the material, it was assumed that the activated zones would have to be heated from room temperature ($18°C$) to the SMP activation temperature of $25°C$, resulting in a fixed temperature change for the activated zones of $\Delta T = 7°C$.

To investigate the optimal design problem now with localized material activation rather than full activation, a subset of the target shapes from both of the prior test sets were considered: Target Shape 2 (unidirectional sin-wave, Figure 3.4(b)) and Target Shape 4 (distorted sin-wave, Figure 3.9(b)).

3.5.2.1 Localized Material Activation Vs. Full Material Activation To contrast with the previous results with full activation in terms of shape matching accuracy, the solutions from the Pareto front with the lowest Modified Hausdorff distance values were considered in order to compare the design solutions with full material activation to the design solutions with localized material activation in terms of shape matching accuracy. Figures 3.14(a) and 3.14(b) show the value of the Modified Hausdorff distance for the final design shapes obtained from optimizing with respect to the Modified Hausdorff distance with one through four discrete actuators for Target Shapes 2 and 4 for both localized activation and full activation (i.e., the same as those shown in Figures 3.7 and 3.11). Specifically, in Figure 3.14(a) it can be seen that, with the exception of one actuator, the optimization procedure that included localized activation found design solutions that resulted in lower Modified Hausdorff distance values (i.e., better shape matching) for Target Shape 2 than when using full activation. This is due to the pressure being more effectively used, essentially localizing the effect of the pressure. Similarly considering Target Shape 4 (Figure 3.14(b)), the optimal designs utilizing localized material activation resulted in lower Modified Hausdorff distance values for every design case. The design solutions using localized actuation were even capable of improving the shape matching for Target Shape 4 using less actuators (e.g., one actuator with localized activation was more accurate than four actuators with full activation). Thus,

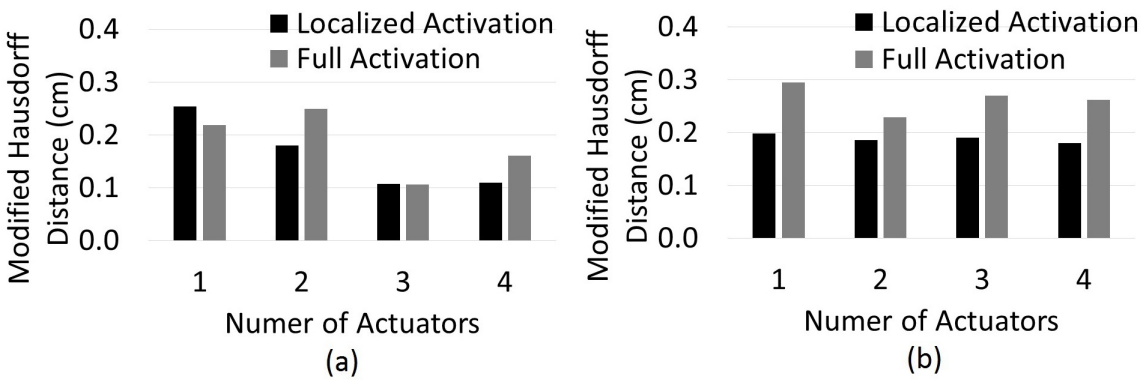

Figure 3.14: Modified Hausdorff distance values for optimal designs for Target Shape 2 (a) and Target Shape 4 (b) using various numbers of actuators with both localized activation (black) and full activation (gray).

there is clear benefit to the use of localized activation to achieve improved shape matching of a smart material morphing structure. Moreover, the use of less actuators to achieve a more accurate shape indicates that the use of localized activation is not only beneficial for shape matching purposes but also does so with a lower energy cost in terms of both thermal activation and mechanical actuation.

3.5.2.2 Trade-off between Shape Changing Accuracy and Energy Cost Figure 3.15 shows the composite Pareto fronts in terms of the total energy cost and final Modified Hausdorff distance for the potential designs obtained from the multi-objective optimization for Target Shapes 2 and 4 These composite Pareto fronts were constructed from the final populations of potential design solutions for each case of one through five actuators. One method for choosing the preferred solution (i.e., single optimal solution) from a Pareto front is to select the solution that is nearest to the origin along the front. The two optimal design

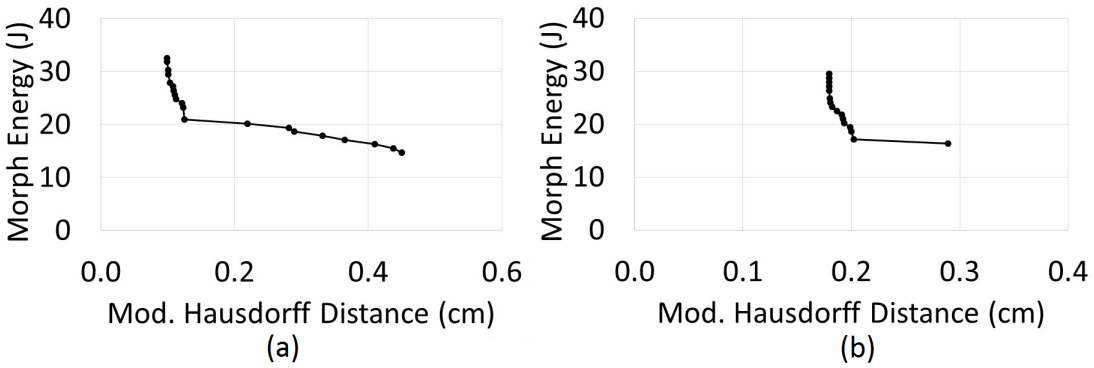

Figure 3.15: Trade-off between the two objective functions, the Modified Hausdorff distance (x-axis) and morphing energy cost (y-axis) for Target Shape 2 (a) and Target Shape 4 (b).

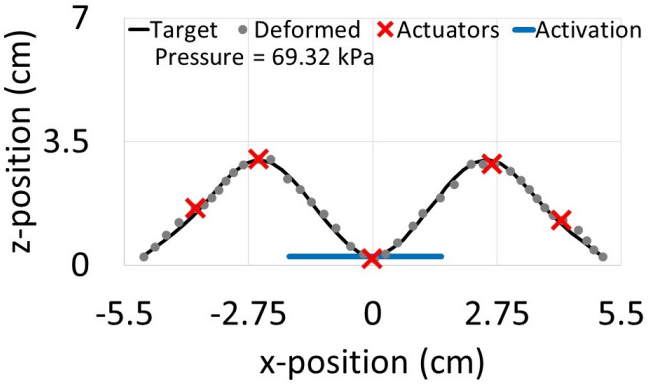

Figure 3.16: The morphed tile shape for the "best" design solution, target shape, and actuator placement (a) as well as the thermally activated zones (b) for Target Shape 2.

solutions (one for each Target Shape) that were nearest to the Pareto front origin are shown in terms of the deformed shapes, actuator placements, and activated zones in Figures 3.16 and 3.17.

Both Pareto fronts corresponding to Target Shape 2 and 4 show a distinct point of diminishing returns in terms of both objectives, with each Pareto front having a clear L-shape. For example, for Target 2 in order to reduce the energy cost by 30% from the optimal solution on the L-shaped curve the accuracy of the shape matching must be reduced by 173%. Similarly, in order to improve the shape matching accuracy by 4% from the optimal solution, the energy cost increases by 17%. To examine the design solutions further, the relative contribution of the mechanical actuation and the material activation to the morphing energy cost was examined for each case. It was found that the material activation

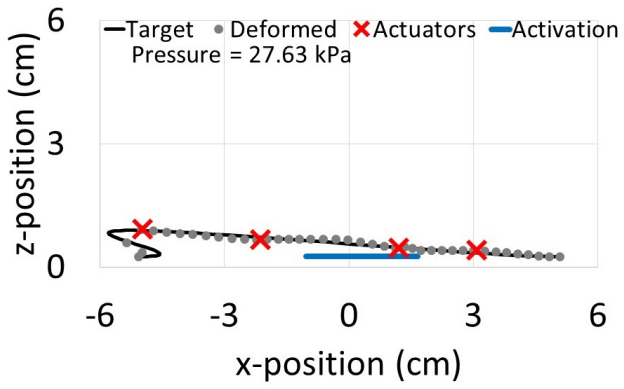

Figure 3.17: The morphed tile shape for the "best" design solution, target shape, and actuator placement (a) as well as the thermally activated zones (b) for Target Shape 4.

energy cost was significantly greater than the mechanical actuation energy cost in all cases, but the extent of which was dependent on the number of actuators utilized for the design. Specifically, when one actuator was utilized the thermal energy cost was greater than 90% of the total energy cost while it was as low as 60% of the total energy cost while utilizing five actuators. Thus, there were at times highly non-intuitive outcomes in balancing the number of actuators, total energy cost, and shape accuracy. Further related to energy efficiency, Figures 3.16 and 3.17 show that even though 20 separate activated zones ($m = 20$) could be utilized, the push for efficiency naturally led to smooth (i.e., a small number of continuous activated regions rather than a large number of small activated zones) results, and in affect, regularized the solution (eliminating the need for regularization of the parameterization). In the case of Target Shape 4, the activated region is located near the center of the tile, which is not an intuitive solution. This is due to the strain energy due to extension is higher than the strain energy due to bending, therefore applying the activation to the section to be extended results in a higher reduction in strain energy. Looking more closely at the Pareto front corresponding to Target Shape 2 (Figure 3.15(a)), the solutions clustered around the point nearest the Pareto front origin generally utilized three or five actuators, while the solutions with higher Modified Hausdorff distance values and lower energy cost utilized a mixture of one, two, and four actuators. Considering the Pareto front corresponding to Target Shape 4 (Figure 3.15(b)), it was found that all solutions with a Modified Hausdorff

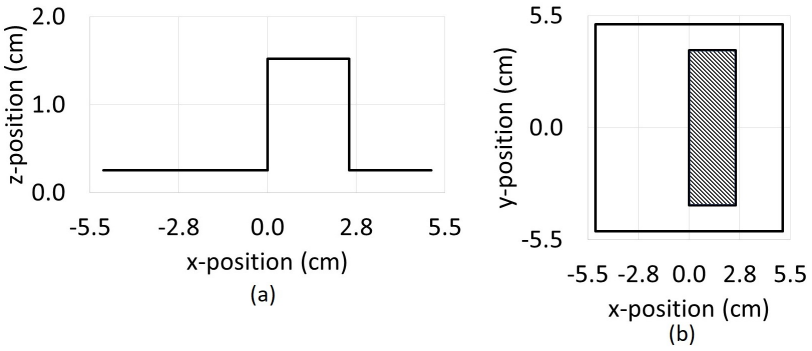

Figure 3.18: (a) A cross-sectional view and (b) a top view for the 3D target shape (a boxcar function), with the hatched section being the raised portion of the target shape.

distance below 0.19 cm utilized four actuators, while the remainder utilized two actuators. Again, the fluctuations in the solutions are non-intuitive in comparison to the previous single objective optimization and indicate the necessity of a computational approach for maximum shape matching and energy cost benefits.

3.5.3 Three-Dimensional Target Shape

For this group of numerical case studies, the same approach for the design optimization as the first group of tests was used (interior point algorithm minimizing shape difference) with the Modified Hausdorff distance used as the objective function. The variable parameterization was also mostly the same as prior examples, with the exception of removing the discrete actuators in order to reduce the complexity of the design space (i.e., the only actuation was the applied pressure). The activation was defined by a set of circular regions on the 3D tile, activating uniformly through the thickness as before, with controllable center locations and diameters. Differing from the previous two groups of tests (which had 2 fixed edge faces and 2 free edge faces), all four outer edge faces were fixed to have zero displacement in all directions.

Figure 3.18 shows the target shape, a boxcar function extended to three dimensions. The boxcar of the 3D target shape had a height of 1.27 cm and was centered on the lines $x = 1.27$ cm and $y = 0$ cm with a width of 2.54 cm and a length of 7.62 cm. This 3D target

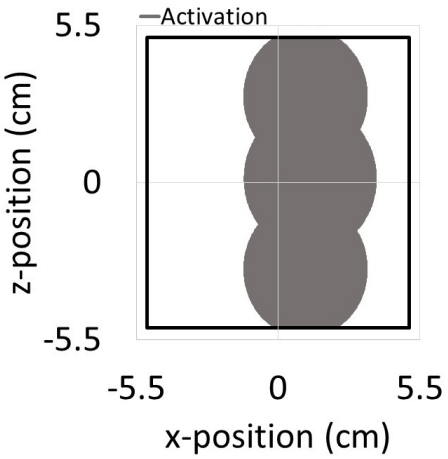

Figure 3.19: The activated (gray) and unactivated (white) portions of the tile for the final design solution for the 3D target shape.

shape was chosen to be similar to an overhang shape (a common shading device).

Figure 3.18 shows the location of the activated material for the final design solution. These activated regions are concentrated over the location of the boxcar portion of the target shape, which is consistent with what would be expected given the constraints on the design problem. The Modified Hausdorff distance between the deformed model surface and the 3D target shape for this design solution was 0.20 cm. A plot of a cross-section (taken at $y = 0$ cm) of the 3D target shape and the deformed model surface of the design solution is shown in Figure 3.20. In this case the design optimization was not able to reach a solution

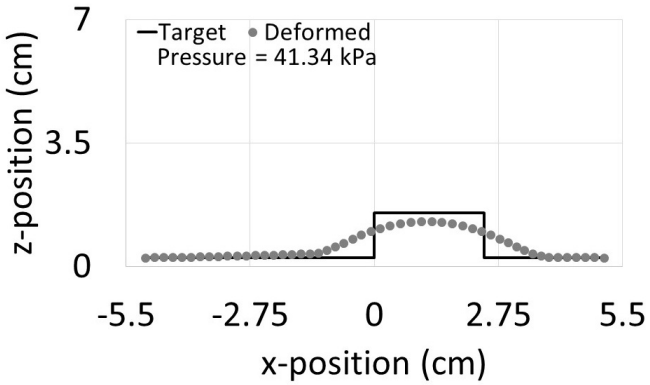

Figure 3.20: The morphed tile shape for the design solution and 3D target shape.

with the sharp features of the 3D target shape. This is due to only using a uniform pressure which will always result in a smooth, continuous solution. However, the Modified Hausdorff distance of 0.20 cm can be considered a small value, particularly in comparison to the prior examples in Section 3.5.1.1, which has Modified Hausdorff distance values of 0.20 cm for two or more actuators. Furthermore, although the deformed tile is observably different than the 3D target shape, this design solution still resembles an overhang, which was the goal of choosing the target shape in the first place.

3.6 Conclusions

The development and evaluation of a computational approach for optimal design of a smart material shape changing building skin tile was presented. This approach was evaluated through numerical examples that considered the capability of the computational procedure utilizing various shape-based objectives and design variable parameterizations to accurately match a target shape. The results indicated that the computational approach utilizing the shape-based objective functions can result in mechanisms of morphing that lead to accurate deformed shapes in comparison to various target shapes. Of the shape metrics considered, the Modified Hausdorff distance was shown to be preferable because the computational approach utilizing the Modified Hausdorff distance resulted in the most consistently accurate shape matching. Additionally, the computational approach utilizing the Modified Hausdorff distance was applicable to any shape, even target shapes without a one-to-one vertical projection, while retaining acceptable deformed shape accuracy. The results also indicated that the use of localized material activation for the design of a smart material shape changing structure of the type considered here can lead to higher accuracy in matching target shapes (i.e., better functionality) than a design that only has the capability to activate the entire structure. However, the design space for the system considered had a significant trade-off between shape matching accuracy and energy cost. Yet, the ability to use localized activation for the design was shown to require considerably less energy to perform the shape change and to require less actuation devices, potentially benefiting implementation considerably.

4.0 Design, Prototyping, and Evaluation of a Concept for a Shape-Changing Smart Material Building Surface Tile

4.1 Overview

A design concept for shape-changing smart material tiles for applications in environmentally responsive building facades is presented. In particular, the application considered is a tile that would change the shape of the building surface to favorably affect the interaction with solar irradiance. A lab-scale prototype system for smart material tiles composed of 3D printed thermally responsive shape memory polymer (SMP) and utilizing localized thermal material activation and uniform pressure actuation is examined. Tests utilizing the prototype tile are used to create and validate a computational (finite element) representation of the adaptive surface tile system. Towards developing this computational representation, a strategy is presented to determine and validate the material parameters for the 3D printed SMP by matching the tile shape predicted by the numerical model to the tile shape measured experimentally. This numerical representation was then implemented into a computational approach to explore the design space for this adaptive tile to have an effect on the solar irradiance on a building surface. More specifically, a series of numerical examples are considered that determine the location and size of material activation that minimize the area of the tile exposed to solar irradiance. Results indicate that the adaptive tile can change the surface of a structure to considerably improve the structure's interaction with solar irradiance. Additionally, the importance of the control strategy for a multi-tile system was displayed, particularly with respect to the capability to significantly reduce the energy cost and affect the solar irradiance to a higher degree by accounting for neighboring tile interaction.

4.2 Introduction

Energy consumption in the United States is dominated by the commercial building sector at 40% of total energy, and within the commercial building sector the main consumers are lighting and HVAC systems [3]. Due to this, there has been a considerable effort in recent research to reduce energy demand in commercial buildings. Specifically, many of these efforts focus on allowing the building to adapt to internal and external stimuli. Examples of interior building technologies include reducing energy consumption with occupancy sensors for light control [86], or predictive control for ventilation and HVAC systems [87]. Recently, focus has begun to switch to external building technologies, and an example of which is responsive building skins, which change configuration based on an environmental stimulus [32, 34, 36, 39].

Responsive building skins have been recently developed to reduce the energy consumption of all main energy consumers within commercial buildings [59]. In an effort to reduce HVAC demand within Media-TIC building in Barcelona an inflatable skin was implemented that inflates portions of the skins based on light sensors to increase insulation [32]. Alternatively the Heliotrace system [32] and the responsive building skin of the Al Bahard towers [34] utilized a series of mechanical apertures to control the flow of light into their respective buildings. Even more recent work has been considering the possibility of including a variety of smart material technologies to further expand the potential capabilities of responsive building skin technologies. The use of smart materials has several potential benefits, due to their controllable (i.e., programmable) intrinsic property changes and the ability to use naturally occurring stimulus (e.g., heat or solar radiation) or minimal supplied energy to elicit these property changes. Utilizing one or both of these smart material capabilities can lead to smart components that have more adaptivity and/or require less energy to achieve the same level of adaptivity, while also potentially eliminating overall system complexity (e.g., removing the need for hinges, etc.).

There are several smart material technologies that have been implemented into external building structures in order to mechanically change the façade, similar to the example of the Al Bahard towers [34], to allow the building to positively interact with environmental stimuli.

For example, in [88] shape memory alloy actuators that were activated when the external temperature reached a predefined level were used to deform portions of a façade. Specifically, portions of the façade would create openings for increased airflow, and would then close once the temperature decreased below the activation threshold. Some examples have constructed environmentally responsive façade components that were instead comprised entirely of smart material, rather than just attaching smart material components to a standard material façade element [35, 36, 39]. A specific example of a façade component comprised of a smart material was explored in [39] which utilizes hygromorphic materials, which behave similarly to a conifer cone in nature when the relative humidity changes [39]. This allows the façade component to "close" and provide shelter during high moisture loads (i.e., rain) and "open" to allow solar exposure during low moisture loads. Alternatively, Barrett et al. developed a building skin that used bimetal sheet layers that had differing coefficients of thermal expansion in order to curl towards or away from the structure based on the thermal loading in the surrounding environment [35, 36]. The curling behavior of the façade component reduced solar gains by providing shading during high thermal loading and increased insulation during periods of low thermal loading. These examples where the façade components are comprised of the smart material themselves, as well as the majority of applications of smart materials within building façade systems in general, have used naturally occurring stimulus alone to illicit the adaptivity. The primary benefit of using naturally occurring stimulus is that no additional energy is required to activate the system. Although, this means that the system is entirely dependent on the environment, which is an issue if the desired behavior is not perfectly correlated with an environmental stimulus.

There have been several applications of smart materials for structures and structural components where active activation (i.e., energy from a man-made source) was used, rather than activation from the natural environment, and the overall performance of the structure still improved [89–94]. One example within building structures involved piezoceramic smart materials [94], which produce an electric charge when subjected to a stress or strain (and the converse effect). In this example, thin wafer piezoceramic sensors were placed (singly or stacked) on a structure to first determine vibrations based on electricity output, and then electrically activated to dampen the vibrations. Additionally, several examples of structures

utilizing active smart material activation are present in aeronautical applications [89–93]. For example, actively activated smart material actuators were used to change the shape of wings or blades based on flight plans which allowed aircraft to efficiently adapt to conditions or changes in flight plans (e.g., ascent, descent, increase speed, decrease speed). Utilization of smart materials to change the shape of aircraft wings has simplified the morphing process, resulted in more economic builds, and required less maintenance than previous methods that used standard engineering materials. While active activation does require an additional energy cost, it is an acceptable cost for many applications to allow for more complex behavior of smart material structures. Furthermore, by providing additional functionality it is possible that and the overall energy savings can be greater with active activation regardless of the cost.

The current study presents a concept for a shape-changing smart material building surface tile that will change shape for optimal interaction with solar exposure. The shape-changing tile façade is entirely comprised of smart material (as opposed to being actuated by smart materials). Active material activation, based on the positioning of the sun, is considered to provide a fully controllable façade with diverse functionality. For the proposed shape-changing tile, the shape-change is achieved through a localized activation of the smart material paired with a uniform pressure to deform the activated ("soft") portion(s) of the tile. The objective of this study is to experimentally and numerically investigate the capabilities of this shape-changing tile concept. As such, a physical prototype of the tile concept was developed using a shape memory polymer as the smart material. This prototype was then used to develop, calibrate, and validate a numerical representation (finite element model) of the tile based on experimental results. A design concept utilizing the numerical representation was developed and evaluated through numerical case studies in the context of reducing the area of a building exterior in solar exposure. In the following section, details of the benchtop experiments are given, including the manufacturing of the shape memory polymer tiles, the test apparatus setup, experimental procedure, and evaluation of the experimental results. A general computational representation of the smart material building skin tile is

developed and presented in Section 3 as well as details on material model calibration and model validation. Numerical examples, their results, and discussion are then given in Section 4, which is followed by concluding remarks in Section 5.

4.3 Adaptive Smart Material Tile Design Concept

The design concept considered herein is an adaptive shape changing "wrinkled" surface tile based upon the prior work developing building surface "cactus tiles" by Clifford [41]. The original cactus tile objective from the previous work was to have static "wrinkled" surface tiles that were both aesthetically pleasing and had functional benefits in terms of self-shading. However, it is envisioned that adding the capability of such tiles to change between wrinkle patterns, would further enhance the original benefits and potentially include many other functional behaviors [41, 72, 73]. The proposed mechanism to produce a tile that can morph between different wrinkle patterns (i.e., shape changing cactus tile) is envisioned to be controllable localized activation of the smart material comprising the tile (e.g., softening) and mechanical actuation to deform the tile into a desired shape. Localized material activation has been shown to improve the efficiency of a shape-changing structure [70] and is utilized as an additional control variable to increase functionality of the shape-changing building surface tile.

4.3.1 Benchtop Prototype

A physical prototype of the design concept was developed to explore the practical feasibility and provide the experimental results from which to develop a numerical representation for further evaluation. This prototype was developed with a thermally responsive shape memory polymer (SMP) as the smart material. It should be noted that the SMP used for the prototype is not proposed as the preferred material for actual construction, but allowed

Figure 4.1: Printed SMP material.

rapid prototype development and is representative of the morphing capability that would be desired as further development and material selection occurred. The following details the process to construct and test the morphing capability of the SMP tile.

4.3.1.1 SMP Tile Printing The SMP tile was created using 3D printing of a polyurethane filament provided by SMP Technologies Inc. [95]. A standard 3D printer, a Creator Pro Dual Extrusion 3D printer by Flashforge, was used for the printing process. The printing software utilized was Matter Control with settings of infill speed, top solid infill speed, support material speed, and travel speed of 30 mm/s, inside and outside perimeters speeds of 25 mm/s, extruder temperature of 210°C, and bed temperature of 48°C. The resultant tile had an activation temperature, T_g, of 55°C [82, 83]. Figure 4.1 shows an example of the printed SMP tile material. In particular, it can be seen that the printing process prints alternating layers of horizontal and vertical alignment, which yielded an isotropic overall material behavior.

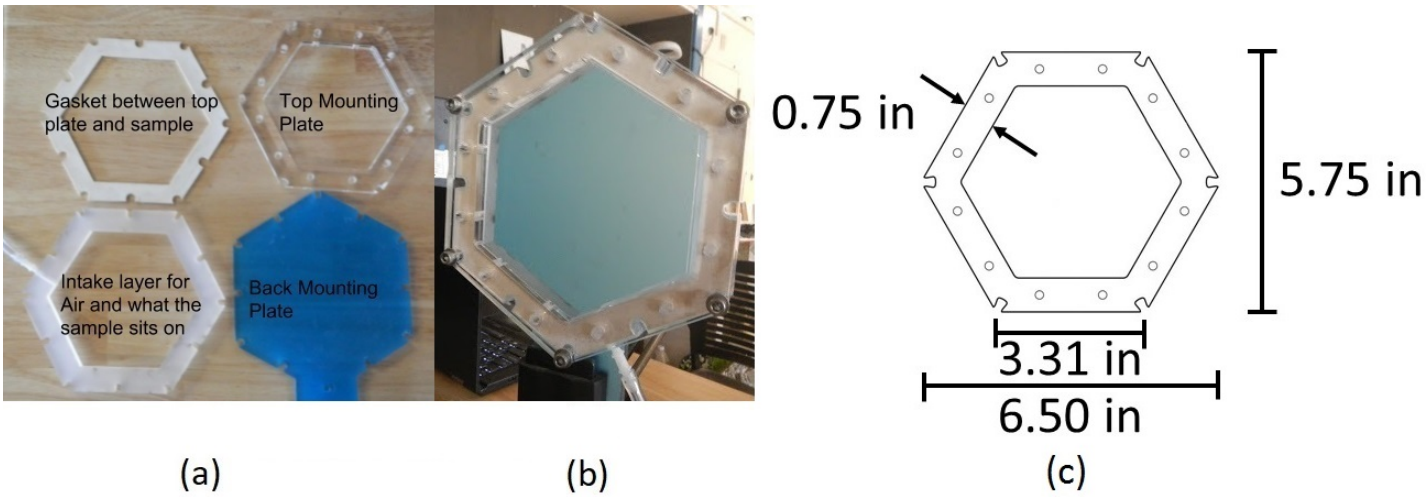

Figure 4.2: The test apparatus that was used to evaluate the SMP tile morphing, including (a) the layers of the apparatus, (b) the fully assembled apparatus, and (c) the dimensions of the apparatus.

4.3.1.2 Test Apparatus and Morphing Procedure Figure 4.2 shows the apparatus used to test the SMP tiles and evaluate their morph capability, including a breakdown of the apparatus components and dimensions. Acrylic plates were used to frame the tile, with an entry point for pneumatic actuation in the back. This allowed for a uniform pressure to be applied by a compressor to deform the tile following material activation. The SMP tile was bolted into the test jig using 12 #8 machine screws, ensuring an air tight seal. The tile was then actuated through the use of a constant pressure, 10 psi, applied by the compressor. Next, the tile was heated by a Milwaukee Heat Gun (1400 W) until the T_g of 55°C was reached (confirmed using a FLIR infrared camera). As the temperature of the SMP rises the stiffness of the material decreases allowing deformation under uniform pressure. The application of uniform pressure was not removed until the tile was cooled and "locked" into place. Photographs of the deformed shape were taken by a digital camera in order to extract the surface deformation for input into solar analysis software and to develop the computational framework.

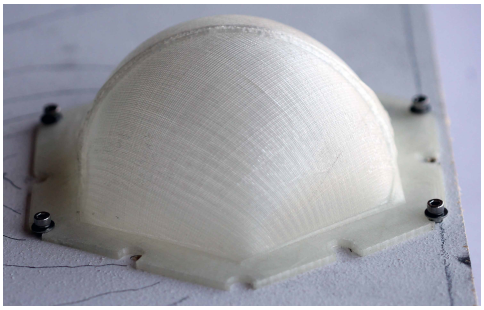

Figure 4.3: Deformed fully activated SMP tile with uniform pressure.

4.3.2 Experimental Test Cases

Two experimental tests were performed using the procedure described in Section 4.3.1.2. In the first experiment, the entirety of the tile was heated to T_g (referred to as "fully activated"). Figure 4.3 shows an example of the deformed shape of the fully activated tile. This morphed fully activated tile had an expected rotationally symmetric positive Gaussian curvature "hemispherical" shape. In the second experiment the heat gun was localized to a single location on the tile, resulting in an approximately circular portion of the tile being activated (referred to as "locally activated"). The locally activated tile with constant pressure resulted in an asymmetric deformed tile shape. The resultant deformation of these tiles, both fully and locally activated, was found to be recoverable and repeatable without any indications of damage.

4.3.3 Shading Potential of Deformed SMP Tiles

Although a more refined evaluation of the design concept was performed using a numerical representation, the experimental results from the prototype were used to perform a preliminary evaluation of the self shading potential of the design concept, particularly the use of localized activation to affect the amount of self-shading with respect to the position of the sun. Specifically, the shading profile of both the fully and locally activated tiles, as if they were vertically mounted on an unobstructed South facing wall, were determined for three times on June 21^{st} 2015: 09:00, 12:00, and 15:00. The shading profiles were determined using Rhinoceros 3D [96] with time, date, location, and an object file (i.e., the deformed shape

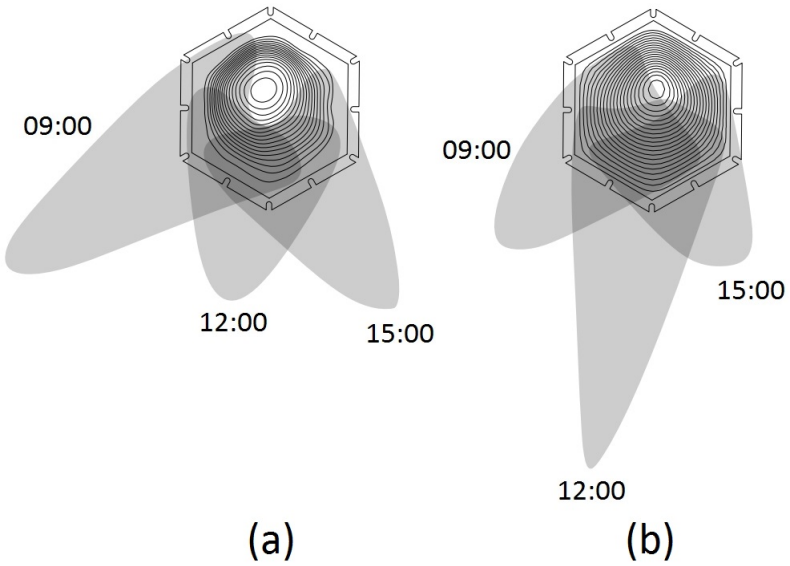

Figure 4.4: Shading profiles for the (a) fully activated and (b) locally activated tiles at 09:00, 12:00, and 15:00 on June 21st 2015.

of the tile) as input. The shape of the fully activated tile was held constant for all three times, whereas, the shape of the locally activated tile was changed by rotating the tile so that the peak of the deformed shape was in-line with the position of the sun and the center of the tile. Figure 4.4 shows the shadow cast by the morphed tile for both fully activated and locally activated cases, noting that the locally activated case had a different location of activation for each of the three time points. For all times both the fully and locally activated tiles provided significant self-shading, as well as shading beyond the boundaries of the tile. Specifically, the location of material activation in the locally activated tile had a large effect on the shadow cast in comparison to the fully activated tile. Moreover, the locally activated tile requires less activation energy than the fully activated tile thereby reducing overall energy costs of the system.

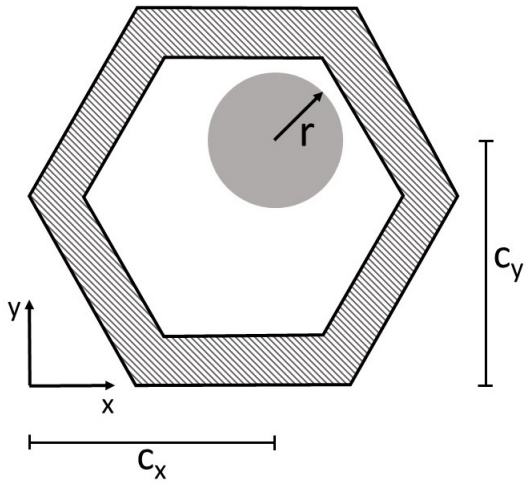

Figure 4.5: Schematic of the tile concept where activated material is gray and unactivated material is white.

4.4 Computational Smart Material Tile Representation

Utilizing the observations from the physical experiments with the benchtop prototype, a numerical representation of the smart material tile was developed with standard finite element analysis. Figure 4.5 shows a schematic of the tile and the parameters defining material activation. The numerical representation of the tile was defined with the same dimensions as those shown in Figure 4.2(c) with a thickness of 0.1 in. The shape changing process was assumed to be quasi-static. The outer 0.75 in were taken to be fixed with zero displacement in all directions, while all other faces were free to deform due to the actuation pressure being applied. The material was assumed to be instantaneously activated so that regions of the tile were either activated or inactivated completely (i.e., no transition zones). The SMP tile was assumed to be an isotropic Neo-Hookean hyperelastic material with a fixed Poisson's ratio of 0.45 (i.e., nearly incompressible). The Young's modulus of the unactivated tile material (i.e., glassy modulus) was observed to have a minimal effect on the deformed tile shape (provided it was sufficiently higher than the Young's modulus of the activated tile material). Therefore, the glassy modulus was fixed at a value of 150 ksi based on the reported literature [82]. Most importantly, for the finite element analysis to be representative of the

experimental prototype it was necessary to estimate the activated tile Young's modulus and validate the assumption of the circular activated region based on the experimental results. It should be noted the numerical determination of the activated tile Young's modulus was required due to experimental limitations that did not allow for material characterization.

4.4.1 Calibration and Validation Procedure

The calibration and validation of the numerical representation of the smart tile was performed using an optimization-based inverse problem solution strategy based on the work in [72, 73]. The inverse problem was to estimate the unknown tile material parameters and the activated material distribution to match the shape of the tile measured through the associated experimental test of the prototype. Therefore, the inverse problem could be cast as the following constrained optimization problem:

$$\begin{aligned} \underset{\vec{\gamma}}{\text{minimize:}} \quad & MH_d\left(S_T, S_F(\vec{u})\right) \\ \text{subject to:} \quad & F(\vec{u}, \vec{\gamma}) = 0 \\ & \vec{b}_l \leq A(\vec{\gamma}) \leq \vec{b}_u, \end{aligned} \tag{4.1}$$

where S_T is the target surface shape, S_F is the predicted morphed shape of tile as defined by the deformation of the tile, $\vec{u}$, estimated by the finite element analysis of the forward problem (FEBio software, with standard TET10 elements), $F(\vec{u}, \vec{\gamma}) = 0$ (i.e., the partial differential equation constraint), for a given set of parameters, $\vec{\gamma}$ (which will be defined in the respective cases), $MH_d(\cdot, \cdot)$ is the metric that quantifies the difference between two shapes, $\vec{b}_l$ and $\vec{b}_u$ are the lower and upper bound constraint vectors, respectively, and $A(\vec{\gamma})$ is the operator that forms the necessary constraint equations involving the activation parameters. The metric to quantify the difference between two shapes, $MH_d(\cdot, \cdot)$, was the Modified Hausdorff distance [78]. This metric was chosen due to positive results in previous work [72] in matching a shape changing tile model to a predefined target shape. The Modified Hausdorff distance is calculated for two discretized shapes, S_1 and S_2, as:

$$MH_d(S_1, S_2) = \max(M(S_1, S_2), M(S_2, S_1)) \tag{4.2}$$

where:

$$M(S_1, S_2) = \frac{1}{N_1} \sum_{i=1}^{N_1} \min_{\vec{x_2} \in S_2} \parallel \vec{x_{1i}} - \vec{x_2} \parallel, \tag{4.3}$$

$\vec{x_1}$ and $\vec{x_2}$ are the Euclidean coordinates of the i^{th} points on shapes S_1 and S_2, respectively, N_1 is the total number of points on S_1, and $\parallel \cdot \parallel$ is the standard Euclidean distance. This Modified Hausdorff distance is analogous to an L_2 norm and ensures that every point on each shape contributes to the distance metric [78].

A standard gradient-based interior point optimization algorithm [97] was utilized. For each inverse solution estimation, the gradient-based optimization was repeated ten times, with a new randomly generated initial solution guess each time. The stopping criteria for each optimization process was set to be when the change in objective function between iterations fell below a tolerance value of 10^{-6}. The final estimate for the inverse solution was then chosen as the result out of the ten with the lowest Modified Hausdorff distance value.

4.4.1.1 Calibration and Validation Results First, the unknown Young's modulus of the activated SMP tile was determined by applying the inverse solution procedure to the test results for the case with the fully activated tile. Therefore, $\vec{\gamma}$ is the Young's modulus of the activated material ($\gamma = E_T$). The result of the inverse solution estimation for all ten random starting points (approximately 0.1% difference between solutions) was a Young's modulus of approximately 341 *psi*. The Modified Hausdorff distance between the deformed tile surface estimated by the finite element model with the inverse solution for Young's modulus and the surface extracted from the experiment was 0.148 *in*. A 3D plot and cross-sectional view of the deformed tile surface estimated by the finite element model with the inverse solution for Young's modulus and the surface extracted from the experiment can be seen in Figure 4.6. This Modified Hausdorff distance that was less than 3% of the tile height was deemed to be sufficiently accurate, and thus, the inverse solution for the Young's modulus was sufficiently accurate.

The activated Young's modulus value found was used in the proceeding test to determine the accuracy of the localized material activation design variable parameterization. For the second test the Young's modulus of the activated material is known, therefore the variable $\vec{\gamma}$ is set equal to the activation parameters ($\vec{\gamma} = \{c_x, c_y, r\}$), where c_x is the x-coordinate of the

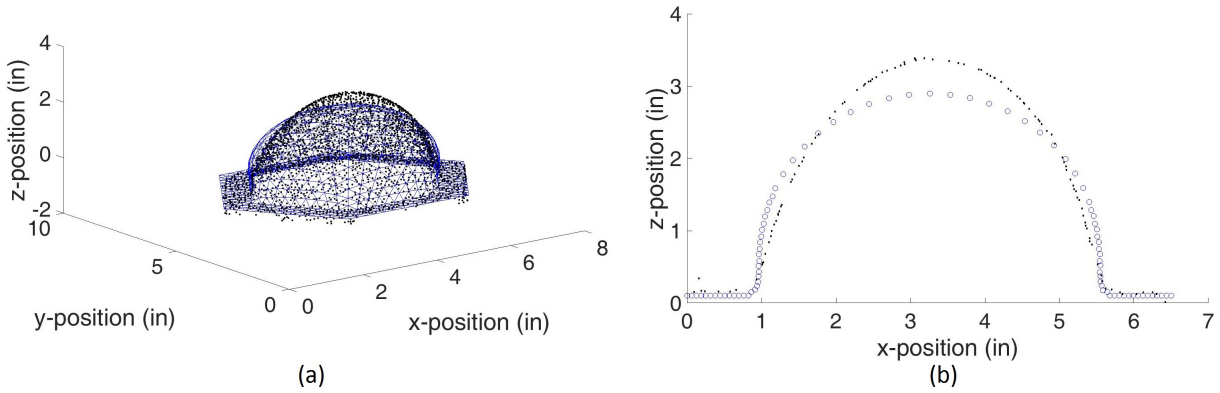

Figure 4.6: A (a) 3D view and (b) cross-sectional view (taken at $y = 0$) of the extracted surface of the fully activated experimental tile (blue) and the surface extracted from the model with the estimated Young's modulus (black).

center of activation, c_y is the y-coordinate of the center of activation, and r is the radius of activation (as shown in Figure 4.5). The solution for all ten random starting points resulted in a Modified Hausdorff distance between the deformed tile surface estimated by the finite element model and the surface extracted from the locally activated tile experiment of 0.09 in, which was judged to be sufficiently accurate (less than 2% of the tile height). A 3D plot and cross-sectional view of the deformed tile surface estimated by the finite element model and the surface extracted from the experiment can be seen in Figure 4.7. The material activation parameters for the optimal solution were the center point of activation being located at $(3.74\ in, 3.11\ in)$ and the radius of activation being 1.89 in. This solution results in the upper right-hand quadrant of the tile being activated which is consistent with the location of activation in the experimental tile.

As stated previously, the preliminary goal of this design concept was to increase the shaded area of the building envelope (or reduce the area in solar exposure). In order to determine if the numerical representation was accurately representing the design concept, the shading potential of the extracted surface of the locally activated experimental tile and the resultant surface of the numerical tile must be determined. To compare the extracted experimental surface and the resultant surface from the numerical representation for the locally activated tile an algorithm that was developed in [73] was used to determine the

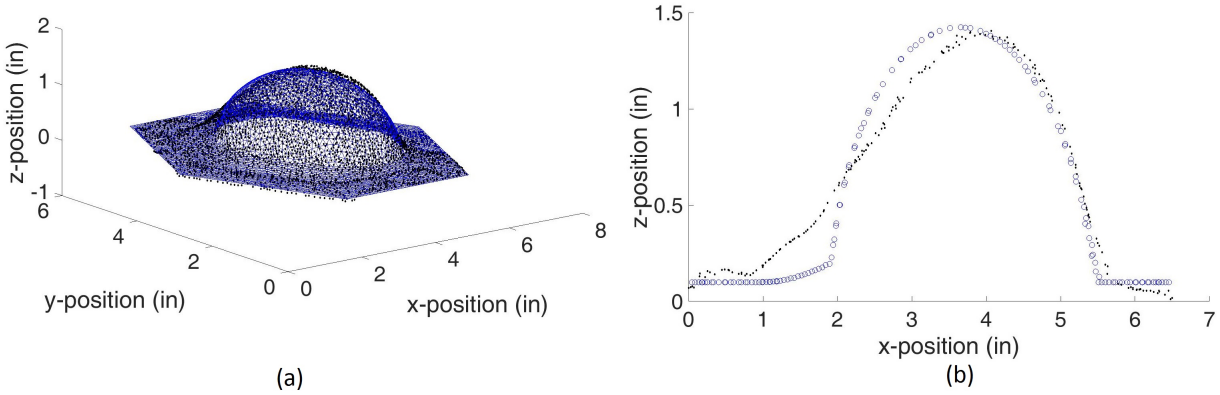

Figure 4.7: A (a) 3D view and (b) cross-sectional view (taken at $y = 0$) of the extracted surface of the locally activated experimental tile (blue) and the surface extracted from the locally activated tile model (black).

percentage of shaded area for these two surfaces on July 21^{st}, 2015. The extracted experimental surface resulted in 35.4% of the tile surface area in shade, while the resultant surface from the numerical representation resulted in 32.6% of the tile surface area in shade. This difference in shaded area was judged to be within acceptable limits, which indicated that the model accurately represented the design concept and could be used to explore the potential capabilities further.

4.5 Self-Shading Capability of the Smart Material Building Surface Tile

The validated numerical representation was utilized to investigate the potential capabilities of the adaptive self-shading smart material design concept through a series of numerical case studies. These case studies were intended to investigate not just the self-shading capability of the design concept, but also implementational aspects, including the frequency of morphing (e.g., hourly, daily, or monthly shape changes) and the interaction of neighboring tiles if installed as an array (as opposed to a singular tile). A computational design optimization procedure was applied to each test case to determine the size and location of the circular region of localized activation to minimize the area of the tile exposed to solar

irradiance. This design optimization utilized the same procedure as was used for the inverse solution estimation described in Section 4.4, with the exception of the objective function. The objective function in Equation 4.1 was replaced for the optimal design process with the following:

$$\underset{\gamma}{\text{minimize:}} \quad \sum_{i=1}^{n_t} E_A\left(t_i, S_F(\vec{u})\right) \tag{4.4}$$

where n_t is the number of times used to estimate solar exposure, t_i is the i^{th} time of interest, and $E_A(\cdot,\cdot)$ is the metric that quantifies the area exposed to solar irradiance for the given tile shape and dependent upon the chosen date, geographic location (latitude and longitude), vertical location, and tile orientation (again, this was calculated using the algorithm from [73]). Minimizing the area of the tile exposed to solar irradiance was chosen as an objective due to the relationship between temperature, radiated energy, and conducted energy, even though this would increase the temperature of the areas exposed. As the temperature of a smaller area increases it also increases the energy radiated off of the surface rather than being conducted into the building. For all the proceeding tests it was assumed that the theoretical tiles were vertically mounted on an unobstructed South facing wall in Phoenix, Arizona (latitude of 33.45° and longitude = −112.07°, with positive latitude being North and positive longitude being East). A final important consideration not yet mentioned for the design of this type of smart material shape changing structure is to ensure that the design solution does not damage the structure. Although a constraint could be included in the design optimization problem to prevent solutions that damage the material [70], preliminary tests showed this to be unnecessary for the case studies considered. However, the final design solutions were still checked to ensure no damage of the material would occur by confirming the maximum principal strain anywhere in the deformed SMP tiles did not exceed damage limits of 30% for inactivated material or 400% for activated material.

4.5.1 Numerical Case Studies for a Single Tile

For the single tile numerical case studies, the focus was to determine the effect of different morphing frequencies. Specifically, hourly, daily, and monthly morphing frequencies were considered. For this first case study the area of tile exposed to solar irradiance was calculated

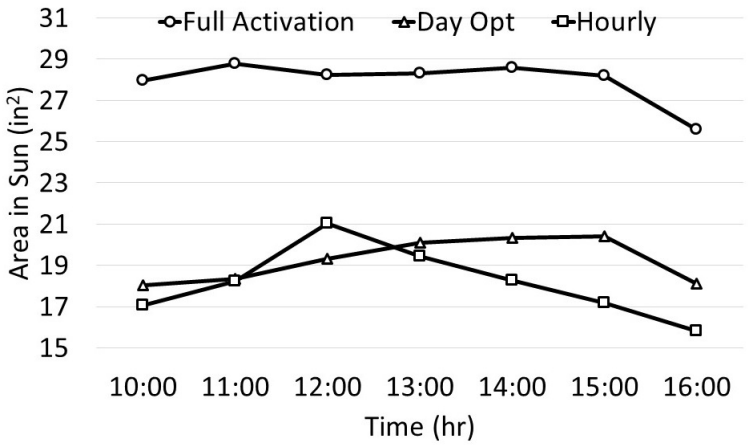

Figure 4.8: Area of solar exposure with respect to time for the fully activated tile (circle), daily optimized tile (triangle), and hourly optimized tile (square).

for the timespan of 10:00-16:00 on July 21^{st}, 2015 for three different tile control methods. The first control method was a tile that does not change (i.e., a static tile) that has the shape of the fully activated tile from the previous investigation (Figure 4.6) (referred to as "fully activated tile"). The second control method was a tile that does not change (i.e., a static tile) that has a shape that minimizes the area of tile that is exposed to solar irradiance for the summation of three representative times of the day ($n_t = 3$) of interest (10:00, 12:00, and 14:00) (referred to as "representative tile"). The final control method was a tile that changed hourly (i.e., a dynamic tile) to the shape that minimized the area of the tile that was exposed to solar irradiance at the beginning of the hour ($n_t = 1$) of interest (referred to as "hourly tile"). Figure 4.8 shows the area of solar exposure for the timespan of 10:00-16:00 for the fully activated tile, the representative tile, and the hourly tile. Specifically, the representative tile and the hourly tile resulted in an average of 31.2% and 35.1% less exposed area, respectively, than the fully activated tile. Additionally, the hourly tile resulted in an average decrease of 5.6% exposed area compared to the representative tile. Furthermore, there is one time point (12:00) where the representative tile results in the least tile area exposed to solar irradiance. This is likely due to the fact that the representative tile shape was optimized to minimize solar exposure for not only this time, but also times around 12:00 as well.

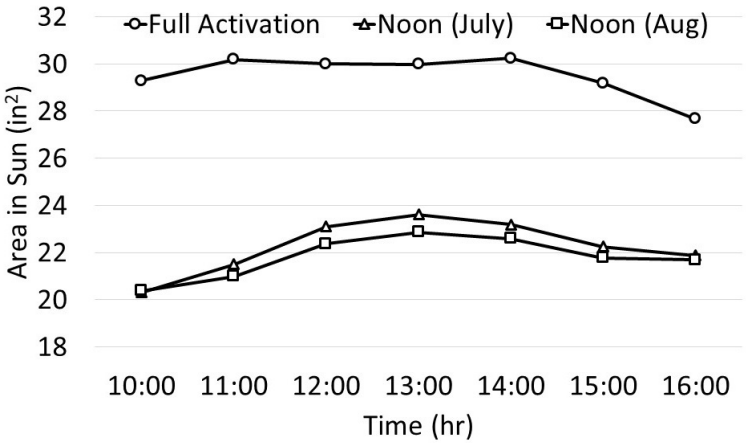

Figure 4.9: Area of solar exposure with respect to time for the fully activated tile (circle), the tile optimized for noon in July (triangle), and the tile optimized for noon in August (square).

For the second case study the solar exposure was calculated for the timespan of 10:00-16:00 on August $21^{st}, 2015$ for three different tile control methods. The first control method was again a tile that does not change (i.e., a static tile) that has the shape of the fully activated tile from the previous investigation (Figure 4.6) (referred to as "fully activated tile"). The second control method was a tile that does not change (i.e., a static tile) that has a shape that minimizes the area of tile that is exposed to solar irradiance at noon on July $21^{st}, 2015$ (referred to as "July tile"). The final control method was a tile that does not change (i.e., a static tile) that has a shape that minimizes the area of tile that is exposed to solar irradiance at noon on August $21^{st}, 2015$ (referred to as "August tile"). Figure 4.9 shows the area of solar exposure for the timespan of 10:00-16:00 for the three tile control cases. The July and August tiles resulted in an average of 24.5% and 26.1% less exposed area, respectively, in comparison to the fully activated tile. The August tile resulted in an average decrease of 2.0% exposed area compared to the July tile. These results indicate that increasing the morphing frequency results in a larger decrease in area exposed to solar irradiance. It can also be seen that the closer to winter the date is (the sun has a lower elevation angle) the overall exposed area will increase (the solar angle is closer to the normal of the building surface). Thus, a flat tile is preferred during winter months to minimize the

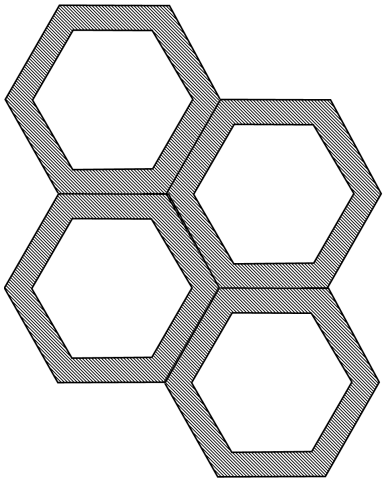

Figure 4.10: The "honeycomb" arrangement of the array of tiles.

area of the tile exposed to solar irradiance.

4.5.2 Numerical Case Study for an Array of Tiles

For the final set of numerical case studies, the performance of the tile in an array setting was investigated to assess potential interactions in the shading provided by neighboring tiles and how the control process may be changed due to these interactions. Specifically, a two-by-two array in a "honeycomb" configuration was used, as shown in Figure 4.10. Similarly to the single tile investigation, the array of tiles was assumed to be mounted onto a South facing wall in Phoenix, Arizona on July $21^{st}, 2015$. Four different cases were considered which will be defined by the control method of the array and how the shape of the array was determined. In the first array considered all four tiles were controlled together (i.e, all tiles in the array were the same shape) to take the shape of the fully activated tile from Section 4.4.1.1 (referred to as "fully activated"). In the second array considered all four tiles were controlled together to take the shape that minimizes the area of a single tile exposed to solar irradiance at 12:00 on July $21^{st}, 2015$ (from Section 4.5.1) (referred to as "dependent control single tile design"). In the third array considered all four tiles were controlled together to take the shape that minimizes the area exposed to solar irradiance for the entire array at 12:00 on July $21^{st}, 2015$ (referred to as "dependent control array design"). In the final

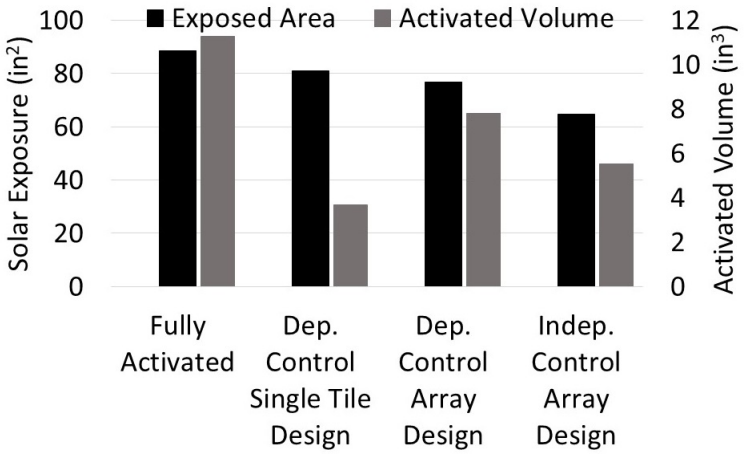

Figure 4.11: Area of solar exposure and volume of material activation for the fully activated array, dependent control single tile design, dependent control array design, and independent control array design.

array considered all four tiles were controlled independently (i.e., potentially four different tile shapes) to take the shape that minimizes the area exposed to solar irradiance for the entire array at 12:00 on July $21^{st}, 2015$ (referred to as "independent control array design"). Additionally, for each array of tiles the volume of activated material was calculated as well in order to have an indication of the energy required for the morphing process.

Figure 4.11 shows the area of solar exposure at 12:00 on July $21^{st}, 2015$ and volume of activated material for all four arrays considered. Figure 4.11 shows that the dependent control array design and independent control array design resulted in less area exposed to solar irradiance than the fully activated array and the dependent control single tile design. Specifically, the dependent control array design resulted in more than 5% decrease in exposed area in comparison to the fully activated array and the dependent control single tile design and the independent control array design resulted in more than 20% decrease in exposed area in comparison to the fully activated array and the dependent control single tile design. This indicates that minimizing the area exposed to solar irradiance for the entire array (as opposed to a singular tile) results in a larger decrease in area exposed to solar irradiance. Additionally, the independent control array design resulted in 15% less exposed area than the dependent control array design, which indicates that controlling the tiles independently

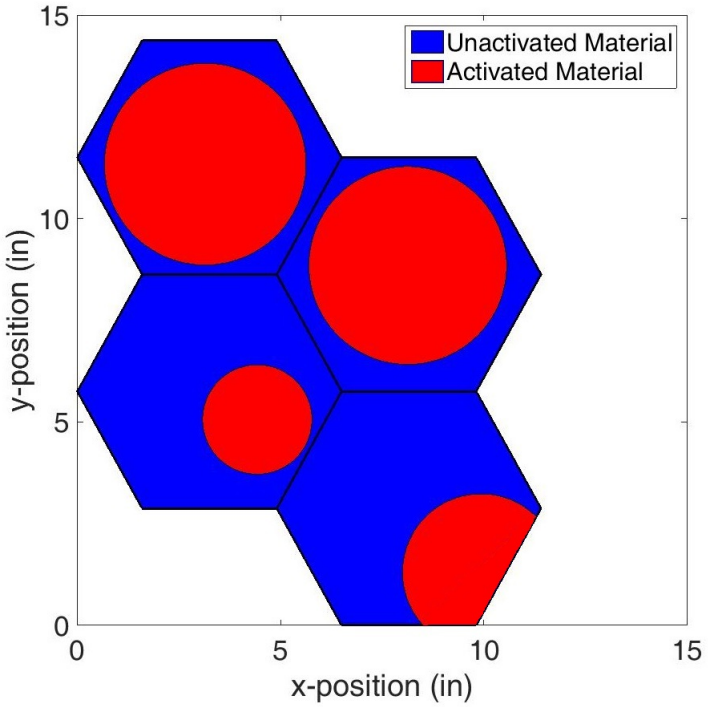

Figure 4.12: Top view of the unactivated (blue) and activated (red) material for the array of tiles for the independent control array design.

(i.e., potentially all different tile shapes), as opposed to controlling the tiles dependently (i.e., all tiles are the same shape), is more beneficial in terms of reducing the area exposed to solar irradiance. In terms of activation volume the independent control array design resulted in 29.2% less activated volume that that of the dependent control array design. As an example, Figure 4.12 shows the activated material distribution for the independent control array design. The activation is primarily located in the upper tiles of the array. This is due to the optimization of the independent control array design recognizing that tiles closer to the sun provide shading for the subsequent tiles, therefore, the subsequent tiles do not need to be activated to the same extent. This results in a large portion of the array not needing activation thereby reducing the energy required to provide shading for the array of tiles.

4.6 Conclusions

The design concept of a shape-changing smart material building skin tile was presented in the context of reducing solar irradiance entering a building. The concept was initially explored through experimental tests that explored localized smart material activation. A numerical model of the shape-changing tile was developed, calibrated, and validated based on the experiments and was then implemented within a computational approach with the purpose of designing the morphing mechanisms of the tile. The computational approach for the design of this tile was evaluated through numerical examples that considered the capability of the computational procedure utilizing localized material activation to optimally interact with solar exposure. The results indicated that the design of the physical tile can be accurately represented by the computational approach. Additionally, it was shown that the morphing frequency (i.e., hourly, daily, monthly, etc.) has a significant effect on the area of the tile exposed to solar irradiance. Finally, it was determined that if the tiles are arranged in an array configuration controlling the tiles independently from one another not only leads to less tile area being exposed to solar irradiance but also requires less tile area to be activated.

5.0 Current Capabilities and Future Directions

A concept for a shape-changing smart material building surface tile was presented. Three primary investigations were performed: quantification of the self-shading capabilities of the shape-changing tile, development and evaluation of a computational design strategy for design of the morphing mechanisms of a shape-changing smart material tile, and development and numerical evaluation of a benchtop prototype shape memory polymer tile. Throughout this work was an overarching effort to develop a computational inverse problem framework for the design of the morphing mechanisms of a shape-changing smart material tile. To develop this framework, several numerical tools were created and/or implemented to address the wide range of problem requirements. An algorithm was created for determining the area of an object (discretized into a finite element mesh) exposed to solar irradiance based on back-ray tracing. A method was implemented for quantifying the shape difference between a target surface shape and a surface estimated by a numerical representation of the tile based on the Modified Hausdorff distance. An algorithm was also created for automatic material definition within the numerical representation of the tile based on the localized material activation parameters.

Currently the framework is capable of determining the optimal mechanical actuation and thermal activation necessary to minimize the difference between the estimated tile surface shape and various target shapes. Specifically, accurate design solutions can be found for target shapes both with and without a one-to-one vertical projection. Furthermore, design solutions can also be found when minimizing both shape difference and morphing energy. Additionally, the framework is capable of determining optimal thermal activation parameters to minimize the area of the tile exposed to solar irradiance. Furthermore, two different optimization methods were tested within the framework. For single objective optimization (minimize shape difference or area of solar exposure) a gradient-based interior point algorithm was used and for multi-objective optimization (minimize energy in addition to one of the previous objectives) a controlled, elitist genetic algorithm was used. It should be noted

that no gradient was supplied for the single objective optimization (finite difference method was used for calculation of a gradient). Finally, the framework is capable of calibration of activated material parameters if provided experimental data.

In terms of the overall building tile concept, future work can be directed towards further verification of the concept as well as further developed and implementation of the concept. Specifically, numerical or physical investigation into the quantification of the change in solar gains of a building that utilizes the shape-changing tile concept would aid in verification of the overall concept. Additionally, further work could be focused on implementational aspects that weren't considered in this work (such as automated material activation method, scaling the problem to the size of a building, and construction methods). In terms of the computational approach developed, certain implementational aspects of the approach can be modified to increase the accuracy and efficiency of the approach. Specifically, the forward model analysis method and the optimization objective functions utilized can be improved. Currently, the forward model analysis method being used (finite element method) is inefficient for problems that contain large deformations (such as those considered in this work) due to requiring small mesh sizes and possibly remeshing. As a means to increase efficiency and accuracy of the forward model mesh-free methods, which do not suffer from the mesh instabilities that standard finite element method does, could be implemented. The optimization objective functions currently being utilized are not differential and therefore the finite difference method is utilized to calculate a gradient which increases computational expense and can require more iterations to reach a solution. In future work differentiable forms of the Modified Hausdorff distance and solar irradiance can be developed and implemented for increased efficiency of the approach.

Appendix

Computational Approach Efficiency

A.1 Two Step Optimization Procedure

A challenge when using an optimal design strategy, such as the one previously presented, is that the partial differential equation (PDE) constrained optimization must be solved any time a shape change is desired. Therefore, the computational expense could potentially be a limiting factor for how often the shape of a structure can change. Increasing the computational efficiency of this approach could significantly contribute to facilitating more frequent shape changing, and therefore, an overall more efficient structure. The direct solution of this problem (determining actuation and activation to minimize the area exposed to solar irradiance) is computationally expensive due to having to solve a forward problem at every step.

A way to improve the efficiency is to use a two step optimization process as opposed to the direct solution utilized previously. The first step of the two step optimization process would replace the PDE constraint with an ad hoc constraint based on how the tile deforms. The second step would then solve the forward model (PDE constraint) with the addition of an initial starting point provided by the solution of the first step. The addition of a starting point provided by the solution of the first step is expected to result in less evaluations of the forward model and therefore higher computational efficiency. This solution method is reliant on being able to determine the shapes that the tile can achieve.

Similar to the previous work the design strategy considered herein was based on utilizing non-linear optimization in combination with a numerical representation of the shape-changing tile to be designed. As noted previously the approach was split into two optimization steps. The goal of the first step was to determine the tile shape that minimizes the area of the tile exposed to solar irradiance. Based on observations of previous results

from Chapter 4 the possible shapes of the tile were estimated as a tile with a hemispherical extrusion (specifically a hemisphere scaled down to 60%) at a variable planar location with a variable radius. This first step can be written in the general form of the following constrained optimization problem:

$$\begin{aligned} \underset{\vec{\gamma}}{\text{minimize:}} \quad & E_A\left(t, \vec{\gamma}\right)) \\ & \vec{b}_l \leq A(\vec{\gamma}) \leq \vec{b}_u, \end{aligned} \tag{.1}$$

where t is the time of interest, $\vec{\gamma} = \{c_x, c_y, r\}$ is the vector of parameters that define the hemispherical region, and $E_A(\cdot, \cdot)$ is the metric that quantifies the area exposed to solar radiation (algorithm developed in [73]). Additionally, c_x is the x-coordinate of the hemispherical region, c_y is the y-coordinate of the hemispherical region, and r is the radius of the hemispherical region. The goal of the second optimization step was to determine the the material activation mechanisms that minimize the difference between the resultant tile surface shape from the previous optimization step and the resultant shape from the numerical representation of the tile (similar to the approaches in Sections 3.4 and 4.4.1.1. Additionally, this second step will utilize the design variables from the design solution of the previous step as a starting point for the material activation parameters. This second step can be written in the general form of the following constrained optimization problem:

$$\begin{aligned} \underset{\vec{\beta}}{\text{minimize:}} \quad & MH_d\left(S_T, S_F(\vec{u})\right) \\ \text{subject to:} \quad & F(\vec{u}, \vec{\beta}) = 0 \\ & \vec{c}_l \leq B(\vec{\beta}) \leq \vec{c}_u, \end{aligned} \tag{.2}$$

where S_T is the target surface shape (resultant from previous step), S_F is the predicted morphed shape of tile as defined by the deformation of the tile, $\vec{u}$, estimated by the finite element analysis of the forward problem, $F(\vec{u}, \vec{\beta}) = 0$ (i.e., the partial differential equation constraint), for a given set of parameters, $\vec{\beta} = \{a_x, a_y, r_a\}$, $MH_d(\cdot, \cdot)$ is the metric that quantifies the difference between two shapes (the Modified Hausdorff distance used previously), $\vec{b}_l$ and $\vec{b}_u$ are the lower and upper bound constraint vectors, respectively, and $A(\vec{\gamma})$ is the operator that forms the necessary constraint equations involving the activation parameters. Additionally, a_x is the x-coordinate of the center of the activated region, a_y is the

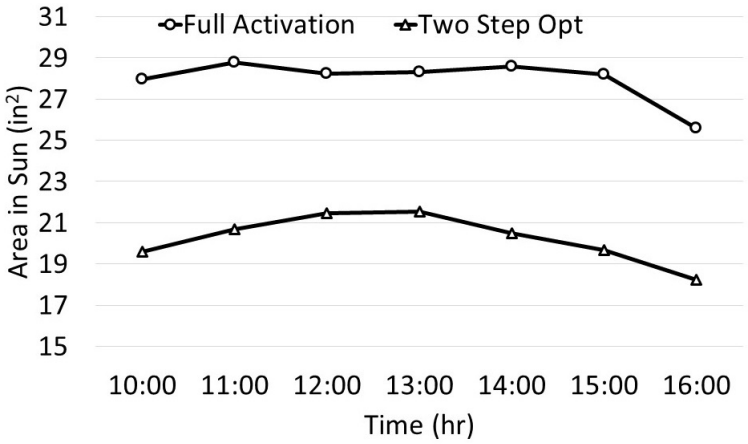

Figure A1: Area of solar exposure with respect to time for the fully activated tile (circle) and the resultant tile from the two step optimization procedure (triangle).

y-coordinate of the of the center of the activated region, and r_a is the radius of the activated region.

A.2 Numerical Case Studies for Two Step Optimization Approach

This two step design strategy was utilized to determine the activation parameters that minimize the area of tile exposed to solar irradiance for the timespan of 10:00 - 16:00 on July $21^{st}, 2015$ (similar to the single tile investigation in Section 4.5.1). Additionally, the area of tile exposed to solar irradiance for the fully activated case (from Section 4.4.1.1) was again calculated (to provide a benchmark). Figure A1 shows the area of solar exposure for the timespan of 10:00-16:00 for the fully activated tile and the resultant tile from the two step optimization procedure. Specifically, the resultant tile from the two step optimization procedure resulted in an average of 27.6% less exposed area than the fully activated tile. This result is similar to the previous computational approach (direct solution method) and was judged to be acceptable. Additionally, it was found that the design solution to the second step of the optimization was, in all cases, equivalent (within 1%) to the initial guess provided by the first step (i.e., the activated region was located at the same planar location as the

hemispherical extrusion with the same radius), which significantly reduced the computational expense of the procedure.

Bibliography

[1] Roy F Hughes and Sunny S Dhannu. Substantial energy savings through adaptive lighting. In *Electric Power Conference, 2008. EPEC 2008. IEEE Canada*, pages 1–4. IEEE, 2008.

[2] Zhongwei Sun, Shengwei Wang, and Zhenjun Ma. In-situ implementation and validation of a CO_2-based adaptive demand-controlled ventilation strategy in a multi-zone office building. *Building and Environment*, 46(1):124–133, 2011.

[3] Renewable Energy. Energy efficiency trends in residential and commercial buildings. 2010.

[4] David Philip Eckel, Thomas James Batko, Mark Richard Walter, William James Rose, Brian Patrick Donlon, and David Abraham Zeichner. Motion sensing system with adaptive timing for controlling lighting fixtures, August 31 1999. US Patent 5,946,209.

[5] Darryl J Bryans and Lance B Jump. Lighting control subsystem for use in system architecture for automated building, October 2 2001. US Patent 6,297,724.

[6] Antoine Guillemin and Nicolas Morel. An innovative lighting controller integrated in a self-adaptive building control system. *Energy and Buildings*, 33(5):477–487, 2001.

[7] Carl-Eric Hagentoft, A Sasic Kalagasidis, SF Nilsson, Marcus Thorin, and AB Ventotech. Mould growth control in cold attics through adaptive ventilation. In *Proceedings of 8th Nordic Symposium of Building Physics*, 2008.

[8] Tahir Ayata, Ertuğrul Çam, and Osman Yıldız. Adaptive neuro-fuzzy inference systems (anfis) application to investigate potential use of natural ventilation in new building designs in Turkey. *Energy Conversion and Management*, 48(5):1472–1479, 2007.

[9] Valentin Gavan, Monika Woloszyn, Frédéric Kuznik, and Jean-Jacques Roux. Experimental study of a mechanically ventilated double-skin façade with venetian sun-shading device: A full-scale investigation in controlled environment. *Solar Energy*, 84(2):183–195, 2010.

[10] Kenneth Ip, Marta Lam, and Andrew Miller. Shading performance of a vertical deciduous climbing plant canopy. *Building and Environment*, 45(1):81–88, 2010.

[11] Takashi Inoue. Solar shading and daylighting by means of autonomous responsive dimming glass: practical application. *Energy and Buildings*, 35(5):463–471, 2003.

[12] Abdelsalam Aldawoud. Conventional fixed shading devices in comparison to an electrochromic glazing system in hot, dry climate. *Energy and Buildings*, 59:104–110, 2013.

[13] I Guedi Capeluto and Carlos E Ochoa. Simulation-based method to determine climatic energy strategies of an adaptable building retrofit façade system. *Energy*, 76:375–384, 2014.

[14] Michele Sauchelli, Gabriele Lobaccaro, Gabriele Masera, and Francesco Fiorito. Smart solutions for solar adaptive façade preliminary studies for an innovative shading device. In *XIX IAHS World Congress,, Milan, Italy*, 2013.

[15] Juan Zhou and Youming Chen. A review on applying ventilated double-skin facade to buildings in hot-summer and cold-winter zone in China. *Renewable and Sustainable Energy Reviews*, 14(4):1321–1328, 2010.

[16] Suresh B Sadineni, Srikanth Madala, and Robert F Boehm. Passive building energy savings: A review of building envelope components. *Renewable and Sustainable Energy Reviews*, 15(8):3617–3631, 2011.

[17] Yan Liu, Jiang Liu, Liu Yang, Liqiang Hou, Mengyuan Wang, and Yuhao Qiao. Cooling effect for integrated application of phase change envelopes and night natural ventilation in western china.

[18] Hatice Sozer. Improving energy efficiency through the design of the building envelope. *Building and environment*, 45(12):2581–2593, 2010.

[19] Dorota Chwieduk. Towards sustainable-energy buildings. *Applied energy*, 76(1):211–217, 2003.

[20] WR Chang. Effect of porous hedge on cross ventilation of a residential building. *Building and Environment*, 41(5):549–556, 2006.

[21] Panagiota Karava, Ted Stathopoulos, and Andreas K Athienitis. Wind-induced natural ventilation analysis. *Solar Energy*, 81(1):20–30, 2007.

[22] LEM Lignarolo, CMJL Lelieveld, and Patrick Teuffel. Shape morphing wind-responsive facade systems realized with smart materials. In *Adaptive Architecture: An International Conference, London, UK, March 3-5, 2011*, 2011.

[23] Ana I Palmero-Marrero and Armando C Oliveira. Effect of louver shading devices on building energy requirements. *Applied Energy*, 87(6):2040–2049, 2010.

[24] Arman Hashemi. Daylighting and solar shading performances of an innovative automated reflective louvre system. *Energy and Buildings*, 82:607–620, 2014.

[25] Marie-Claude Dubois and M Arch. Awnings and solar protective glazing for efficient energy use in cold climates. In *Renewable Energy Technologies in Cold Climates 98 Conference, May*, pages 4–6, 1998.

[26] Robert E Jones. Effects of overhang shading of windows having arbitrary azimuth. *solar energy*, 24(3):305–312, 1980.

[27] Martin Vraa Nielsen, Svend Svendsen, and Lotte Bjerregaard Jensen. Quantifying the potential of automated dynamic solar shading in office buildings through integrated simulations of energy and daylight. *Solar Energy*, 85(5):757–768, 2011.

[28] Liangliang Sun, Lin Lu, and Hongxing Yang. Optimum design of shading-type building-integrated photovoltaic claddings with different surface azimuth angles. *Applied Energy*, 90(1):233–240, 2012.

[29] Seung-Ho Yoo and Heinrich Manz. Available remodeling simulation for a BIPV as a shading device. *Solar Energy Materials and Solar Cells*, 95(1):394–397, 2011.

[30] Yu-Jiu Wang and Po-Chi Hsu. Analytical modelling of partial shading and different orientation of photovoltaic modules. *Renewable Power Generation, IET*, 4(3):272–282, 2010.

[31] Maria Carla Di Vincenzo, Dilay Kesten, and David Infield. Assessment of performance of building shading device with integrated photovoltaics in different urban scenarios. In *Sustainable Energy Technologies (ICSET), 2010 IEEE International Conference on*, pages 1–5. IEEE, 2010.

[32] Y Dewidar, N Mohamed, and Y Ashour. Living skins: A new concept of self active building envelope regulating systems. In *Advancing the Green Agenda; Technology, Practices and Policies Conference–BUID*, pages 1–8, 2013.

[33] Francesco Fiorito, Michele Sauchelli, Diego Arroyo, Marco Pesenti, Marco Imperadori, Gabriele Masera, and Gianluca Ranzi. Shape morphing solar shadings: A review. *Renewable and Sustainable Energy Reviews*, 55:863–884, 2016.

[34] Karen Cilento. Al bahar towers responsive facade/aedas. *ArchDaily,September*, 5, 2012.

[35] Ronald M Barrett and Ronald P Barrett. Thermally adaptive building covering field test. *Procedia Engineering*, 145:26–33, 2016.

[36] Ronald M Barrett and Ronald P Barrett. Thermally adaptive building coverings: Theory and application. In *ASME 2016 Conference on Smart Materials, Adaptive Structures and Intelligent Systems*, pages V002T06A001–V002T06A001. American Society of Mechanical Engineers, 2016.

[37] Ronald M Barrett and Ronald P Barrett. Thermally adaptive building coverings inspired by botanical thermotropism. In *ASME 2016 Conference on Smart Materials, Adaptive Structures and Intelligent Systems*, pages V002T06A008–V002T06A008. American Society of Mechanical Engineers, 2016.

[38] Zoltan Nagy, Bratislav Svetozarevic, Prageeth Jayathissa, Moritz Begle, Johannes Hofer, Gearoid Lydon, Anja Willmann, and Arno Schlueter. The adaptive solar facade: from concept to prototypes. *Frontiers of Architectural Research*, 5(2):143–156, 2016.

[39] Artem Holstov, Ben Bridgens, and Graham Farmer. Hygromorphic materials for sustainable responsive architecture. *Construction and Building Materials*, 98:570–582, 2015.

[40] I Guedi Capeluto. Energy performance of the self-shading building envelope. *Energy and buildings*, 35(3):327–336, 2003.

[41] Carnegie Mellon University. Cactus tile concept, 2019. URL `http://cmubiologic.weebly.com/cactus-tile.html`.

[42] J Ehleringer, HA Mooney, SL Gulmon, and P Rundel. Orientation and its consequences for copiapoa (cactaceae) in the atacama desert. *Oecologia*, 46(1):63–67, 1980.

[43] John R Howell, M Pinar Menguc, and Robert Siegel. *Thermal radiation heat transfer*. CRC press, 2015.

[44] RF Yanda and RE Jones. Shading effects of finite width overhang on windows facing toward the equator. *Solar Energy*, 30(2):171–180, 1983.

[45] Chanadda Pongpattana and Pattana Rakkwamsuk. Efficient algorithm and computing tool for shading calculation. *Songklanakarin Journal of Science and Technology*, 28(2): 375–386, 2006.

[46] Michael F Cohen and John R Wallace. *Radiosity and realistic image synthesis*. Elsevier, 2012.

[47] Pat Hanrahan, David Salzman, and Larry Aupperle. A rapid hierarchical radiosity algorithm. In *ACM SIGGRAPH Computer Graphics*, volume 25, pages 197–206. ACM, 1991.

[48] Ibrahim Reda and Afshin Andreas. Solar position algorithm for solar radiation applications. *Solar Energy*, 76(5):577–589, 2004.

[49] Roberto Grena. An algorithm for the computation of the solar position. *Solar Energy*, 82(5):462–470, 2008.

[50] Manuel Blanco-Muriel, Diego C Alarcón-Padilla, Teodoro López-Moratalla, and Martín Lara-Coira. Computing the solar vector. *Solar Energy*, 70(5):431–441, 2001.

[51] Patrick T Mather, Xiaofan Luo, and Ingrid A Rousseau. Shape memory polymer research. *Annual Review of Materials Research*, 39:445–471, 2009.

[52] M Fremond. Shape memory alloy. In *Shape Memory Alloys*, pages 1–68. Springer, 1996.

[53] Thomas W Duerig, KN Melton, and D Stöckel. *Engineering aspects of shape memory alloys*. Butterworth-Heinemann, 2013.

[54] NB Morgan. Medical shape memory alloy applicationsthe market and its products. *Materials Science and Engineering: A*, 378(1):16–23, 2004.

[55] Jaronie Mohd Jani, Martin Leary, Aleksandar Subic, and Mark A Gibson. A review of shape memory alloy research, applications and opportunities. *Materials & Design (1980-2015)*, 56:1078–1113, 2014.

[56] Yanju Liu, Haiyang Du, Liwu Liu, and Jinsong Leng. Shape memory polymers and their composites in aerospace applications: a review. *Smart Materials and Structures*, 23(2):023001, 2014.

[57] Ben Dietsch and Tat Tong. A review-: Features and benefits of shape memory polymers (smps). *Journal of Advanced Materials*, 39(2):3–12, 2007.

[58] Andreas Lendlein and Steffen Kelch. Shape-memory polymers. *Angewandte Chemie International Edition*, 41(12):2034–2057, 2002.

[59] MA Shameri, MA Alghoul, Kamaruzzaman Sopian, M Fauzi M Zain, and Omkalthum Elayeb. Perspectives of double skin façade systems in buildings and energy saving. *Renewable and Sustainable Energy Reviews*, 15(3):1468–1475, 2011.

[60] Carl M Lampert. Chromogenic smart materials. *Materials today*, 7(3):28–35, 2004.

[61] Kazuhiro Otsuka and Clarence Marvin Wayman. *Shape memory materials*. Cambridge university press, 1999.

[62] Kai Yu, Weilong Yin, Shouhua Sun, Yanju Liu, and Jinsong Leng. Design and analysis of morphing wing based on smp composite. In *Industrial and Commercial Applications of Smart Structures Technologies 2009*, volume 7290, page 72900S. International Society for Optics and Photonics, 2009.

[63] Jian Sun, Yanju Liu, and Jinsong Leng. Mechanical properties of shape memory polymer composites enhanced by elastic fibers and their application in variable stiffness morphing skins. *Journal of Intelligent Material Systems and Structures*, 26(15):2020–2027, 2015.

[64] Giulio Molinari, Manfred Quack, Andres F Arrieta, Manfred Morari, and Paolo Ermanni. Design, realization and structural testing of a compliant adaptable wing. *Smart Materials and Structures*, 24(10):105027, 2015.

[65] Benjamin KS Woods and Michael I Friswell. Multi-objective geometry optimization of the fish bone active camber morphing airfoil. *Journal of Intelligent Material Systems and Structures*, 27(6):808–819, 2016.

[66] Kerr-Jia Lu and Sridhar Kota. Design of compliant mechanisms for morphing structural shapes. *Journal of intelligent material systems and structures*, 14(6):379–391, 2003.

[67] Brian Prock, Terrance Weisshaar, and William Crossley. Morphing airfoil shape change optimization with minimum actuator energy as an objective. In *9th AIAA/ISSMO Symposium on Multidisciplinary Analysis and Optimization*, page 5401, 2002.

[68] Howoong Namgoong, William Crossley, and Anastasios Lyrintzis. Morphing airfoil design for minimum aerodynamic drag and actuation energy including aerodynamic work. In *47th AIAA/ASME/ASCE/AHS/ASC Structures, Structural Dynamics, and Materials Conference 14th AIAA/ASME/AHS Adaptive Structures Conference 7th*, page 2041, 2006.

[69] Seyed Amin Mohaghegh Motlagh. *An Investigation in Structural Shape Morphing by Modulus Variation*. PhD thesis, University of Pittsburgh, 2014.

[70] Shuang Wang and John C Brigham. A computational framework for the optimal design of morphing processes in locally activated smart material structures. *Smart Materials and Structures*, 21(10):105016, 2012.

[71] New Castle University. Hygromorphic tile concept, 2018. URL `https://blogs.ncl.ac.uk/responsive-materials`.

[72] Robert J Zupan, Richard V Beblo, Dale T Clifford, Ankush Aggarwal, and John C Brigham. Design optimization of a self-shading smart material morphing building skin. 2017.

[73] Robert Joseph Zupan, Dale Clifford, Richard Beblo, and John Brigham. Numerical investigation of capabilities for dynamic self-shading through shape changing building surface tiles. *Journal of Facade Design and Engineering*, 6(1), 2018.

[74] Guojun Lu and Atul Sajjanhar. Region-based shape representation and similarity measure suitable for content-based image retrieval. *Multimedia Systems*, 7(2):165–174, 1999.

[75] Dengsheng Zhang and Guojun Lu. Review of shape representation and description techniques. *Pattern recognition*, 37(1):1–19, 2004.

[76] Remco C Veltkamp. Shape matching: Similarity measures and algorithms. In *Shape Modeling and Applications, SMI 2001 International Conference on.*, pages 188–197. IEEE, 2001.

[77] Daniel P. Huttenlocher, Gregory A. Klanderman, and William J Rucklidge. Comparing images using the hausdorff distance. *IEEE Transactions on pattern analysis and machine intelligence*, 15(9):850–863, 1993.

[78] M-P Dubuisson and Anil K Jain. A modified hausdorff distance for object matching. In *Pattern Recognition, 1994. Vol. 1-Conference A: Computer Vision & Image Processing., Proceedings of the 12th IAPR International Conference on*, volume 1, pages 566–568. IEEE, 1994.

[79] Edwin Peraza-Hernandez, Darren Hartl, and Richard Malak. Simulation-based design of a self-folding smart material system. In *ASME 2013 International Design Engineering Technical Conferences and Computers and Information in Engineering Conference*, pages V06BT07A045–V06BT07A045. American Society of Mechanical Engineers, 2013.

[80] Mengyu Wang, Debaditya Dutta, Kang Kim, and John C Brigham. A computationally efficient approach for inverse material characterization combining gappy pod with direct inversion. *Computer Methods in Applied Mechanics and Engineering*, 286:373–393, 2015.

[81] Mohammad Ahmadpoor, Bahram Notghi, and John C Brigham. A generalized iterative approach to improve reduced-order model accuracy for inverse problem applications. *Journal of Engineering Mechanics*, 142(5):04016020, 2016.

[82] Richard Beblo, Korey Gross, and Lisa Mauck Weiland. Mechanical and curing properties of a styrene-based shape memory polymer. *Journal of Intelligent Material Systems and Structures*, 21(7):677–683, 2010.

[83] Jinsong Leng, Xin Lan, Yanju Liu, and Shanyi Du. Shape-memory polymers and their composites: stimulus methods and applications. *Progress in Materials Science*, 56(7): 1077–1135, 2011.

[84] Inc MathWorks. *MATLAB: the language of technical computing. Desktop tools and development environment, version 7*, volume 9. MathWorks, 2005.

[85] MATLAB Users Guide. The mathworks. *Inc., Natick, MA*, 5:333, 1998.

[86] Marie-Claude Dubois and Åke Blomsterberg. Energy saving potential and strategies for electric lighting in future north european, low energy office buildings: A literature review. *Energy and Buildings*, 43(10):2572–2582, 2011.

[87] Jan Širokỳ, Frauke Oldewurtel, Jiří Cigler, and Samuel Prívara. Experimental analysis of model predictive control for an energy efficient building heating system. *Applied energy*, 88(9):3079–3087, 2011.

[88] Marco Formentini and Stefano Lenci. An innovative building envelope (kinetic façade) with shape memory alloys used as actuators and sensors. *Automation in Construction*, 85:220–231, 2018.

[89] Robert G Loewy. Recent developments in smart structures with aeronautical applications. *Smart Materials and Structures*, 6(5):R11, 1997.

[90] Ermira J Abdullah, Cees Bil, and Simon Watkins. Application of smart materials for adaptive airfoil control. *AIAA paper*, (2009-1359), 2009.

[91] Victor Giurgiutiu. Review of smart-materials actuation solutions for aeroelastic and vibration control. *Journal of Intelligent Material Systems and Structures*, 11(7):525–544, 2000.

[92] S Barbarino, R Pecora, L Lecce, A Concilio, S Ameduri, and L De Rosa. Airfoil structural morphing based on sma actuator series: numerical and experimental studies. *Journal of Intelligent Material Systems and Structures*, 22(10):987–1004, 2011.

[93] Friedrich K Straub and Robert J King. Application of smart materials to control of a helicopter rotor. In *Smart Structures and Materials 1996: Industrial and Commercial Applications of Smart Structures Technologies*, volume 2721, pages 66–78. International Society for Optics and Photonics, 1996.

[94] Gangbing Song, Vineet Sethi, and H-N Li. Vibration control of civil structures using piezoceramic smart materials: A review. *Engineering Structures*, 28(11):1513–1524, 2006.

[95] SMPtechno. Shape memory polymer, smp technologies inc., diaplex, 2018. URL `http://www.smptechno.com/index_en.html`.

[96] Robert McNeel et al. Rhinoceros 3d. *Retrieved Jan*, 15, 2009.

[97] Donald Goldfarb and Shucheng Liu. An o (n3l) primal interior point algorithm for convex quadratic programming. *Mathematical Programming*, 49(1-3):325–340, 1990.